

# Relative Sensitivities of Simulated Rainfall to Fixed Shape Parameters and Collection Efficiencies

Sean W. Freeman<sup>1</sup>, Adele L. Igel<sup>1,2</sup>, Susan C. van den Heever<sup>1</sup>

<sup>1</sup>Department of Atmospheric Science, Colorado State University, Fort Collins, Colorado

<sup>2</sup>Department of Land, Air, and Water Resources, University of California, Davis, Davis, California

Corresponding Author: Sean W. Freeman ([sean.freeman@colostate.edu](mailto:sean.freeman@colostate.edu))

Keywords: Regional and Mesoscale Modelling, Clouds, Convection, Microphysics, Rainfall, Atmosphere, Bulk Parameterization, Shape Parameter

## Abstract

Rainfall prediction by weather forecasting models is strongly dependent on the microphysical parameterization being utilized within the model. As forecasting models have become more advanced, they are more commonly using double-moment bulk microphysical parameterizations. While these double-moment schemes are more sophisticated and require fewer *a priori* parameters than single moment parameterizations, a number of parameter values must still be fixed for quantities that are not prognosed or diagnosed. Two such parameters, the width of the rain drop size distribution and the choice of collection efficiencies between liquid hydrometeors, are examined here. Simulations of deep convective storms were performed in which the

This article has been accepted for publication and undergone full peer review but has not been through the copyediting, typesetting, pagination and proofreading process, which may lead to differences between this version and the Version of Record. Please cite this article as doi: 10.1002/qj.3550

collection efficiency dataset and the *a priori* width of the rain drop size distribution (RSD) were individually and simultaneously modified. Analysis of the results show that the *a priori* width of the RSD was a larger control on the total accumulated precipitation (a change of up to 75% over the typical values tested in this paper) than the choice of collection efficiency dataset used (a change of up to 10%). Changing the collection efficiency dataset produces most of the impacts on precipitation rates through changes in the warm rain process rates. On the other hand, the decrease in precipitation with narrowing RSDs occurs in association with the following processes: (a) decreased rain production due to increased evaporation, (b) decreased rain production due to decreased ice melting, and (c) slower raindrop fall speeds which leads to longer residency times and changes in rain self-collection. These results add to the growing body of work showing that the representation of hydrometeor size distributions is critically important, and suggests that more work should be done to better represent the width of the RSD in models, including further development of triple moment and bin schemes.

# 1. Introduction

Research and forecasting models cannot explicitly represent individual hydrometeors and their associated processes. Instead, they must use parameterizations to make bulk representations of hydrometeors and their effects on the dynamics and thermodynamics within each grid box of the model. Modelled precipitation has been shown to be highly sensitive to both the choice of microphysical parameterization and to the assumptions made within a single parameterization. Adams-Selin et al. (2012) found that changing the assumption about graupel and/or hail density within several microphysical parameterizations when simulating a mid-latitude squall line changed the peak storm total precipitation by up to 500%. Further, Igel et al. (2014) showed that when examining single-moment microphysical parameterizations used to simulate both mid-latitude squall lines and within radiative convective equilibrium conditions, that total precipitation showed up to a 200% increase when changing the *a priori* parameters. This uncertainty in precipitation extends to tropical cyclones as well. For example, Brown et al. (2016) demonstrated that using different microphysics parameterizations in simulations of hurricanes changed total rainfall up to 110%. Many other studies have also found a strong variation in the precipitation predicted by models based on their broader choice of parameterization scheme (e.g. Thompson et al., 2004; Grubišić et al. 2005; Morrison et al. 2009; Morrison and Milbrandt, 2010; Varble et al., 2014) or to their more specific choice of parameters within a single scheme (e.g. Gilmore et al., 2004; Thompson et al., 2004; van den Heever and Cotton, 2004; Morrison et al., 2009; Bryan and Morrison, 2012). These results indicate that the sensitivity of rainfall to *a priori* specified parameters in the microphysical parameterization must be understood to improve forecasting of rainfall.

Within numerical models that are used for research and forecasting, the rate of change of the mass of cloud water and rain water (which are typically partitioned by drop size) can be generally represented using the following equations:

$$\frac{\partial q_c}{\partial t} = -ADV + DF + CE - AC - LACR + MLT - IACR - HFZ \quad (1)$$

$$\frac{\partial q_r}{\partial t} = -ADV + DF + CE + AC + LACR + MLT - IACR - HFZ \quad (2)$$

where  $q_c$  is the cloud water mixing ratio ( $\text{g kg}^{-1}$ ),  $q_r$  is the rain water mixing ratio ( $\text{g kg}^{-1}$ ), and the remaining terms represent the sources and sinks for liquid hydrometeors expressed as process rates (all  $\text{g kg}^{-1} \text{ s}^{-1}$ ): ADV is advection of drops from one grid cell to another, DF is diffusion of drops (source/sink), CE is condensation/evaporation (typically cloud source; rain sink), AC is autoconversion of cloud drops into rain drops (cloud sink; rain source), LACR is the accretion of cloud drops by rain drops (cloud sink; rain source), MLT is the melting of ice to liquid (source), IACR is accretion and riming of liquid by falling ice particles (sink), and HFZ is the loss of liquid hydrometeors due to homogenous or heterogeneous freezing (sink). Microphysical parameterizations need to make various assumptions in order to calculate these processes. The sensitivity to two of these assumptions will be examined in this work: (1) the assumption about the width of the rain drop size distribution which directly affects CE, LACR, and IACR; and (2) the collision efficiency (defined in Section 1.2) within the drop collection parameterizations which directly affects AC and LACR. It should be noted that for the remainder of this article, the rain drop size distribution will be referred to as the RSD, whereas general references to drop

size distributions of other hydrometeors, or to the gamma distribution equation as it relates to hydrometeor sizes itself will be referred to as Hydrometeor Size Distribution, denoted by HSD.

### **1.1. Rain drop size distribution**

As described above, the assumptions made about the HSD of hydrometeors impacts many microphysics processes when modelling storms (e.g. Gilmore et al., 2004; van den Heever and Cotton, 2004; Milbrandt and Yau, 2006; Ćurić et al., 2010; Igel and van den Heever, 2017). However, improvements and evaluations of HSDs, especially the representations of the RSD, have been restricted by the relatively infrequent and spatially limited nature of prior observational research. Most observational studies examining the RSD in a statistical sense have been conducted at the ground (e.g. Uijlenhoet et al., 2003; Niu et al., 2009; Friedrich et al., 2015), after raindrops have interacted with turbulent boundary layer air which will change the RSD through evaporation and droplet breakup. Some field campaigns have made in-cloud RSD observations with aircraft, but such observations have been limited in space and time and often only to particular cloud types (e.g. Yuter and Houze, 1997; Freud et al., 2008; Heymsfield et al., 2015). Because of these limitations, it has been difficult to adequately constrain RSDs in microphysical parameterizations, in particular the RSD widths, to observations.

Although the observations of RSDs are spatially and temporally limited, we can still gain some insights into how best to represent their widths from those observations that are available. Marshall and Palmer (1948) presented some of the first observations of rainfall size distribution with changing rain rates, and noted that higher rainfall rates were correlated with broader RSDs.

Niu et al. (2009) deployed a disdrometer in central China in summer 2007 to measure average precipitation rates and RSDs for both stratiform and convective liquid precipitation. They found that narrower RSDs were correlated with lower precipitation rates, and that RSD width was not fixed throughout storm lifetime. Cao et al. (2008) deployed three 2D Video Disdrometers (2DVDs) at the US Department of Energy Southern Great Plains site in northern Oklahoma from May 2005 to 2007 and derived a relationship between the slope of the RSD and its width, but found that this relationship differs from a relationship observed in Florida by Zhang et al. (2001). Further, Uijlenhoet et al. (2003), Bringi et al. (2009), and Friedrich et al. (2015) have all shown that RSD width can vary within a single storm. The observational evidence of RSD width, while limited mostly to near surface levels, suggests that fixing the RSD width *a priori* or using some empirical relationship to derive the RSD width when performing convective storm simulations (as all single and double-moment bulk microphysics parameterizations require) may produce results that do not compare favourably with observations either because the actual RSD width should vary with time or because the empirical function is not universal for all systems and locations.

The requirement that the HSD shape is fixed *a priori* exists partially because individual hydrometeors cannot be simulated using current cloud resolving models due to computational limits. Instead, either continuous probability distribution functions (PDFs) or binned HSDs, where drops are divided into discrete size bins (e.g. Khain et al. 2015), must be assumed to approximate the microphysical processes in the real atmosphere. One continuous distribution, the gamma PDF (the Marshall and Palmer (1948) exponential PDF is a special case of the gamma PDF), is widely used in bulk microphysical parameterizations to represent the size distributions

of hydrometeor species (e.g. Walko et al., 1995; Milbrandt and Yau, 2005a, 2005b; Thompson et al., 2008; Morrison et al., 2009; Saleeby and van den Heever, 2013). Its frequent use is due in part to the fact that this particular PDF has been shown to be a good approximation of observed RSDs (Adirosi et al. 2015, 2016), although it appears that the goodness of fit of this PDF for hydrometeors other than rain has not been extensively examined. Furthermore, moment-based characteristics are easily derived when using this size distribution function.

The complete gamma PDF used to represent HSDs can be represented, within a single grid cell volume, as:

$$N(D) = N_T \frac{\lambda^\nu}{\Gamma(\nu)} D^{\nu-1} e^{-\lambda D} \quad (3)$$

where  $N$  is the number of drops at diameter  $D$  ( $\# \text{ m}^{-3} \text{ mm}^{-1}$ ),  $N_T$  is the total number concentration of drops in the grid volume ( $\# \text{ m}^{-3}$ ),  $f(D)$  is the PDF (here defined as a gamma HSD; output of  $\text{mm}^{-1}$ ),  $D$  is the droplet diameter (mm),  $\Gamma$  is the standard Euler gamma function (unitless),  $\lambda$  is the slope parameter ( $\text{mm}^{-1}$ ), and  $\nu$  is the size distribution shape parameter (unitless), which controls the HSD width when holding the slope parameter constant (which is equivalent to holding the mass mean diameter constant). When using this equation to represent a distribution of hydrometeors, there are three *a priori* unknown parameters:  $N_T$ ,  $\lambda$ , and  $\nu$ , where the latter parameter is one of the parameters of interest in this study. Expression 3 is just one form of the gamma distribution; however, it is equivalent to the other forms that appear in the literature. Figure 1 shows the impacts of changing  $\nu$  while holding the mass mean diameter and total number concentration (and therefore the total mass) constant (at 1 mm and  $10 \text{ cm}^{-3}$ , respectively). Each HSD is labelled  $\nu\#$ , where  $\#$  indicates the value of  $\nu$  used in plotting each

HSD. Higher values of  $\nu$  result in a narrower HSD when holding the mass and number constant, and  $\nu=1$  is equivalent to the Marshall and Palmer (1948) exponential PDF.

Bulk schemes are generally classified based on the number of moments of the continuous PDF that they predict. In single-moment microphysics schemes, the mixing ratio (third moment) is typically (although not necessarily) prognosed, with the total number, slope parameter, and shape parameter being either fixed or diagnosed using an empirical relationship from the mixing ratio. As such, these schemes produce simulations whose solutions are sensitive to the method used to solve for the three unknowns for all hydrometeors (e.g. Gilmore et al., 2004; van den Heever and Cotton, 2004; Snook and Xue, 2008). In contrast to single-moment parameterizations, double-moment parameterizations predict two moments of the distribution, typically the mixing ratio and number concentration, and use these moments to calculate the slope of the HSD and the total number concentration. However, these schemes still require a shape parameter to be specified *a priori*, and this parameter is then either kept constant throughout the simulation (e.g. Meyers et al., 1997), or alternatively may be diagnosed using thermodynamic properties or one of the other prognosed or diagnosed values of the PDF (e.g. Morrison and Grabowski, 2007; Thompson et al., 2008; Morrison and Milbrandt, 2015).

Whereas single and double-moment schemes specify or diagnose the shape parameter, triple moment parameterizations allow for a varying shape parameter, and spectral bin microphysics schemes do not use a shape parameter at all (Ovtchinnikov and Kogan, 2000; Rasmussen et al., 2002; Milbrandt and Yau, 2005b; Lebo and Seinfeld, 2011; Khain et al., 2015). However, these

two approaches, particularly spectral bin microphysics, are too computationally intensive to run in operational settings. Double-moment microphysics schemes are increasingly being developed and/or used in operational forecasting cloud resolving models, such as in the Consortium for Small scale MOdeling- Deutschland model run operationally by the German Deutscher Wetterdienst (COSMO-DE; Barthlott et al., 2017), the High Resolution Rapid Refresh model run operationally by the US National Oceanic and Atmospheric Administration (HRRR; Alexander et al., 2016), and the High Resolution Deterministic Prediction System run operationally by Environment and Climate Change Canada (HRDPS; Milbrandt et al., 2016). In addition to operational numerical weather prediction models, double-moment schemes are also being implemented into climate models, including ECHAM5 (Posselt and Lohmann, 2009) and the Community Atmosphere Model (CAM; Morrison and Gettelman, 2008). Because of the increasingly widespread use of double-moment schemes in operational numerical modelling and climate modelling, the sensitivity of numerical simulations to the range of possible values that the shape parameter may be assigned *a priori* should be thoroughly examined, particularly for applications where such schemes are necessary to predict the characteristics of a wide range of cloud systems over extensive domains without prior knowledge as to what cloud systems will be formed, as in forecasting and climate models. Furthermore, understanding the sensitivity of numerical models to changes in the RSD width compared to other *a priori* parameters, like the assumptions within the drop collection parameterization, can lead to a better understanding of model weaknesses and which factors to focus on improving.

The sensitivity to non-rain HSD widths in numerical models has previously been examined, including Gonçalves et al. (2008) and Igel and van den Heever (2016) who analysed the role of

the cloud HSD width, and Loftus et al. (2014) and Milbrandt and Yau (2005a) who investigated the microphysical responses to changing the hail shape parameter. Milbrandt and Yau (2005a) focused on the impact of the hail shape parameter choice on sedimentation and other processes in a one-dimensional model. While this simple framework is certainly useful for understanding basic process sensitivity, it neglects the storm-scale interactions that a full three-dimensional simulation environment provides. Furthermore, given their focus on hail rather than rain, Milbrandt and Yau (2005a) did not investigate the effects of droplet coalescence, which can be key to understanding the precipitation sensitivities in convective storms. This study aims to address this gap.

Sensitivities to RSD widths have been addressed in part by Cohen and McCaul (2006), Seifert (2008), Wacker and Lüpkes (2009), Posselt and Lohmann (2009), Milbrandt and McTaggart-Cowan (2010), and Naumann and Seifert (2016). Cohen and McCaul (2006) used a single-moment microphysics scheme and varied the shape parameters of many hydrometeor species simultaneously. Seifert, (2008) used a single-column model to examine sensitivities of evaporation of rain drops to RSD widths and proposed a new parameterization changing the RSD width as a function of the mean volume diameter. Wacker and Lüpkes (2009) and Milbrandt and McTaggart-Cowan (2010) focused on drop sedimentation sensitivity to RSD widths in a single-column model. Naumann and Seifert (2016) examined warm rain processes only. Posselt and Lohmann (2009) evaluated the impact of changing the RSD width in the ECHAM5 climate model microphysics, finding that a narrower RSD led to more rain being stored in the atmosphere. However, this study was run at a very coarse resolution and did not analyse the microphysical processes impacted by the changes to the RSD. None of these previous studies

have focused on the impact of the rain shape parameter alone in a high resolution three-dimensional fully interactive simulation of mixed phase cloud systems, nor the relative importance of these changes in comparison to other critical microphysical specifications, such as the collection efficiencies.

## 1.2. Collection Efficiency and Autoconversion Rates

While there are limited observations to validate rain RSDs, collection efficiencies and autoconversion rates (including here autoconversion of cloud and drizzle-sized droplets to rain droplets) have only been constrained by laboratory studies (e.g. Kinzer and Cobb, 1958; Woods and Mason, 1964), theoretical models (e.g. Shafir and Gal-Chen, 1971; Davis, 1972; Jonas, 1972; Klett and Davis, 1973), and direct and large eddy numerical simulations (e.g. Wang et al., 2008; Benmoshe et al., 2012; Chen et al., 2018). While collection efficiencies and autoconversion rates have not been directly observed, they have been demonstrated to be a source of uncertainty within microphysical parameterizations (e.g. Hsieh et al., 2009; Takuro and Toshihiko, 2015).

One of the first representations of autoconversion inside numerical models was proposed by Kessler, (1969), where autoconversion of cloud drops to rain drops is simply represented as some rate  $A$  such that:

$$A = \begin{cases} k_1[q_c - q_{c0}] & q_c > q_{c0} \\ 0 & \textit{otherwise} \end{cases} \quad (4)$$

where  $A$  is the rate of cloud water mass conversion to rain ( $\text{g kg}^{-1} \text{ s}^{-1}$ ),  $k_1$  is some specified rate constant ( $\text{s}^{-1}$ ; this cannot be directly observed),  $q_c$  is the initial amount of cloud water ( $\text{g kg}^{-1}$ ), and  $q_{c0}$  ( $\text{g kg}^{-1}$ ) is some threshold value of cloud water mass above which autoconversion to rain water will occur (Kessler, 1969; Liu and Daum, 2004). While this is one way of representing autoconversion, several other methods have been proposed. Tripoli and Cotton (1980) presented a modified version of the Kessler (1969) scheme, calculating the  $q_{c0}$  threshold value at each timestep and changing the formulation of the autoconversion rate to a more physical representation. Khairoutdinov and Kogan (2000) used an explicit microphysical simulation of marine stratocumulus clouds to derive an empirical autoconversion rate for bulk microphysical schemes without a threshold value. Several other microphysical parameterizations (e.g. Cohard and Pinty, 2000; Saleeby and Cotton, 2004; Milbrandt and Yau, 2005a) use the full stochastic collection formulae, as shown in Berry and Reinhardt (1974) and Feingold et al. (1988), with specified collection efficiencies to allow for more explicit modelling of self-collection of cloud droplets than those schemes based on Kessler (1969) allow.

The collection efficiencies for various sizes and species of hydrometeors have been determined from theoretical, numerical, and laboratory experiments investigating these interactions between two droplets of various sizes. Generally, the collection efficiency of two droplets is defined as:

$$E(r_1, r_2) = E_{coll}(r_1, r_2)E_{coal}(r_1, r_2) \quad (5)$$

where  $E$  is the collection efficiency,  $r_1$  is the radius of the collector drop ( $\mu\text{m}$ ),  $r_2$  is the radius of the collected drop ( $\mu\text{m}$ ),  $E_{coll}$  is the collision efficiency, and  $E_{coal}$  is the coalescence efficiency. In many microphysical schemes and collection kernels,  $E_{coal}$  is set to unity, such that  $E(r_1, r_2) =$

$E_{coll}(r_1, r_2)$  (e.g. Long, 1974; Hall, 1980). However, this is not strictly a good assumption as Beard and Ochs (1984) demonstrated through empirical tests that coalescence efficiency (also known as coagulation or sticking efficiency) decreased below 100% for collector drop radii  $> 50 \mu\text{m}$ .

Two prominent gravitational collection (i.e. without turbulence impacts) efficiency datasets used in current microphysical parameterizations (e.g. Seifert and Beheng, 2001; Saleeby and Cotton, 2008; Thompson et al., 2008; Morrison and Milbrandt, 2010) are derived from the Hall (1980) (hereafter Hall80) and the Long (1974) (hereafter Long74) collision efficiencies (assuming a coalescence efficiency of unity to calculate the collection efficiency). The Hall80 efficiency dataset is based on the collision efficiencies from several numerical and theoretical studies at various drop sizes, and is highly discretized in its design (Shafir and Gal-Chen, 1971; Davis, 1972; Jonas, 1972; Klett and Davis, 1973; Lin and Lee, 1975; Schlamp et al., 1976). On the other hand, Long74 used similar theoretical and numerical studies (Shafir and Gal-Chen, 1971; Klett and Davis, 1973), but instead of leaving the data in a discretized form, fit polynomials to the data and postulated that the collision efficiency is best described as those fit polynomials.

While the Hall80 and Long74 efficiencies are widely used, neither approach includes the effects of turbulence or of changing pressure. Recent efforts have demonstrated that collision efficiencies are substantially impacted by turbulence (e.g. Pinsky et al., 1999; Ayala et al., 2008; Wang et al., 2008). Furthermore, other recent works have indicated that collision efficiencies are impacted by changing pressure (Pinsky et al., 2001), especially collision efficiencies between

drops near cloud and drizzle size (i.e.  $r \leq 100\mu m$ ). It should be noted that all four of these collection efficiency datasets report on the collision efficiency rather than coalescence efficiency, assuming that the coalescence efficiency is unity for their calculation of the collection efficiency. While the collision efficiencies for systems without turbulence can be exactly determined theoretically, the collision efficiencies for turbulent flows are necessarily mean values of a chaotic system. Despite the fact that gravitational collection efficiency datasets can be known with high accuracy, testing the different representations of these values is critical as different parameterizations are still using different representations of these values.

Figure 2 shows the collection efficiencies of four different droplet sizes ( $r = 10, 25, 50,$  and  $100 \mu m$ ) for four different collection efficiency datasets: the Long74, Hall80, Pinsky01 (which includes effects from changing pressure and are displayed as curves at three pressure levels), and Wang and Grabowski (2009; hereafter Wang09; which includes effects from turbulence at two levels). The different characteristics of the datasets are quickly apparent from this figure. While Long74's approach produces the smoothest collection efficiency function over most radii due to its fitted polynomial, it has two problematic ranges in drop size. First, the collection efficiencies when  $r > 50 \mu m$  are set to unity, creating a discontinuity in the collection efficiency function as the fitted function does not necessarily approach unity at  $r = 50 \mu m$ . Second, when the collected drop radius is lower than  $3 \mu m$ , the fitted function values are less than 0 (in this case, those values are not plotted). The Wang09 efficiencies (with curves for turbulent dissipation rates of  $\epsilon = 100$  and  $400 \text{ cm}^2\text{s}^{-3}$ ), which are calculated here by multiplying the turbulent enhancement factor (which ranges from 1 to 36.52) by the collection efficiency given by the Hall80 efficiencies, produces a generally higher collection efficiency

than the gravitational efficiency datasets (except for Long74 whenever  $r > 50 \mu\text{m}$  as described above) as would be expected when including the effects of turbulence. The Pinsky01 curves (denoted P01 for 1000 hPa, 750 hPa, and 500 hPa) produce similar results to the Hall80 and Wang09 efficiency datasets, with slightly smaller efficiencies in most cases. The largest differences between datasets arise when two drops of nearly the same size collide, with the Hall80 and Wang09 efficiencies showing a significantly larger collection efficiency than the other approaches, even reaching values much larger than 1 at certain radii. However, the likelihood that two drops of nearly the same size will collide in a gravitational collection kernel is near zero as their fall speeds are nearly identical, so this change is unlikely to have a large impact on model outcomes unless the turbulent fall speeds are implemented.

The goals of this study are to enhance our understanding of the sensitivity of convective precipitation to changes in the shape parameter for raindrops, as well as to changes in the collection efficiencies used for all liquid species. As demonstrated above, examining the impacts of the shape parameter in a fully 3D simulation of mixed phase clouds, in which the ice phase plays a significant role, has not previously been done. Further, to the authors' knowledge, only limited studies comparing the results of newer collection efficiency tables to older gravitational kernels have been conducted (e.g. Lee and Baik, 2016). While switching to a triple-moment or spectral bin microphysical parameterization will remove the need for an *a priori* shape parameter, both of these approaches to parameterization still require defining collection efficiencies, as well as a way to represent autoconversion, either through a fixed autoconversion rate similar to Kessler (1969) or through a collection equation, which requires collection efficiencies. This study will enhance our understanding as to whether constraining the collection

kernel and / or removing the shape parameter reduces the sensitivity of simulated storms. Such an understanding of whether the collection kernel or shape parameter need to be constrained will assist in guiding the focus of numerical model.

## **2. Materials and Methods**

Fourteen high-resolution numerical simulations were produced to investigate the impact that changing the rain shape parameter and changing the collection efficiencies have on the thermodynamic, microphysical properties, and total accumulated precipitation of a deep convective storm. We used the open-source Regional Atmospheric Modelling System (RAMS) version 6.1.18 to simulate the storms for this study (Cotton et al., 2003; Saleeby and van den Heever, 2013). RAMS is a nonhydrostatic mesoscale model that is frequently used to simulate deep convective storms (e.g. Grasso, 2000; Gaudet and Cotton, 2006; Barth et al., 2007; Lerach et al., 2008; Nair et al., 2013; Federico et al., 2014; Grant and van den Heever, 2014). The model was initialized using a horizontally homogeneous thermodynamic vertical profile (Figure 3) adapted from Gaudet et al. (2006). This sounding was selected because it produces simulations that quickly give rise to a vigorous deep convective storm. The model setup is described in detail in Table 1. The simulations were run for 150 minutes and analysed for 130 minutes, which is when the primary storm updraft velocities fell below  $30 \text{ m s}^{-1}$ , and new convection began developing along the outflow boundaries. The analysis was concluded at 130 minutes in order to focus on the main storm and to avoid any new cold pool-forced storms contaminating the results.

In this work, we will test the use of four collection efficiency datasets: Hall80, Long74, Pinsky01, and Wang09 (Figure 2). While the Hall80, Pinsky01, and Long74 tables are gravitational efficiency datasets and do not include the effects of turbulence, the Wang09 kernel does include this effect at two levels of turbulence:  $\epsilon = 100\text{cm}^2\text{s}^{-3}$  and  $\epsilon = 400\text{cm}^2\text{s}^{-3}$ , where  $\epsilon$  is the mean viscous dissipation rate of the turbulence, and  $\epsilon = 400\text{cm}^2\text{s}^{-3}$  is the more turbulent case. The Wang09 efficiencies are presented as an enhancement factor over gravitational efficiencies, and so for this work, the Wang09 efficiencies are the result of multiplying those efficiencies by the Hall80 efficiencies. While, unlike the assumptions surrounding the RSD, collection efficiencies can be known with high accuracy and recent work (e.g. Pinsky01; Wang et al., 2005) has begun to converge on values for this dataset, many publications have utilized the Long74 and Hall80 datasets and it is important to examine the sensitivities that this work may have to changing collection efficiency datasets. In the remainder of this article, the Wang09 dataset will mean the Wang09 factors at  $\epsilon = 400\text{cm}^2\text{s}^{-3}$  that are multiplied by the Hall80 efficiencies. We acknowledge that in reality the turbulence will change throughout the cloud system and that using a static mean viscous dissipation rate for this dataset is not an exact representation. However, we have selected the more turbulent case, which should show a greater effect on the rainfall processes than the weak case when compared to the gravitational kernels. Note that Pinsky01 and Wang09 includes both changes to the fall speeds and to the collection efficiencies, but this work uses the enhancement to the efficiencies only. The implementation details of the collection efficiency datasets into RAMS is further described in Appendix I.

The RAMS bin-emulating double-moment bulk microphysics parameterization was utilized for these simulations (Meyers et al., 1997; Saleeby and Cotton, 2004; Saleeby and van den Heever, 2013). This parameterization prognoses both mass and number concentration of eight hydrometeor categories: cloud water ( $1.5 < r < 25 \mu\text{m}$ ), drizzle ( $25 < r < 50 \mu\text{m}$ ), rain ( $r > 50 \mu\text{m}$ ), pristine ice, snow, aggregates, graupel, and hail. A gamma HSD is assumed for all hydrometeor types. Sedimentation, autoconversion of cloud droplets to rain, and collection of cloud droplets by all other hydrometeor species are parameterized through the use of look-up tables representing the collection kernel described in Tzivion et al. (1987). These tables are built from bin scheme representations of these processes that allow for drops of different sizes within a distribution to fall at different rates and to have size-dependent collection efficiencies using an *a priori* collection efficiency table (Feingold et al. 1998; Saleeby and Cotton 2008). The different collection efficiency datasets were implemented into the collection kernel look-up tables using the kernel formula in Tzivion et al. (1987). Additionally, the RAMS parameterization outputs include detailed microphysical process rates, which are crucial to understanding the physical effects of changing the rain shape parameter.

The sedimentation process in RAMS is also represented using bin-emulating techniques, which allows for differential fall speeds based on different drop sizes, and is based on Mitchell (1996). This differs from most of the current bulk schemes in which the fall speed of the entire droplet distribution is the same, and is based on a mass-weighted average for the predicted mass, and a number-weighted average for the predicted number. Further information on the details of the RAMS microphysical scheme can be found in Meyers et al. (1997), Cotton et al. (2003), Saleeby and Cotton (2004), and Saleeby and Cotton (2008).

The model setup and homogeneous environmental thermodynamics of all fourteen runs were identical, as described in Table I. Eight of the runs used the Long74 collection efficiencies and changed the rain shape parameter value only, using  $\nu = 1, 2, 3, 4, 6, 8, 10,$  and 15, where  $\nu = 1$  is the same as the exponential Marshall-Palmer HSD (Marshall and Palmer 1948). This range in values was selected to provide a thorough evaluation of previously observed shape parameters in convective storms (Uijlenhoet et al., 2003; Niu et al., 2009). The simulation where  $\nu = 15$  is omitted from the results presented below as it was nearly identical to the results obtained using  $\nu = 10$ . Six runs used the Hall80, Pinsky01, or Wang09 collection efficiency datasets holding a constant  $\nu$  for rain of either  $\nu = 2$  or  $\nu = 10$ . These two shape parameters were chosen as they represent the broadest and narrowest RSD analysed with the exception of the exponential Marshall-Palmer RSD. All of these experiments are summarized in Table II, which indicates the names used for all simulations presented in this work. The shape parameter for cloud droplets and drizzle was set at  $\nu = 3$ , and the shape parameter for all frozen hydrometeor species was set at  $\nu = 2$ . These appear to be reasonable values for each species (e.g. Cohard and Pinty, 2000; Lim and Hong, 2009; Igel and van den Heever, 2017b). All six of the varying shape parameter runs were completed using the Long efficiencies for collision-coalescence and autoconversion. For the remainder of this work, the Long74 simulations will be designated Long $\nu$ #, the Hall80 simulations will be designated Hall $\nu$ #, the Pinsky01 simulations will be designated Pinsky $\nu$ #, and the Wang09 simulations will be designated Wang $\nu$ #, where # is the value of  $\nu$  for rain in all cases.

### 3. Results

The storm evolution can be seen by examining the accumulated precipitation from all simulations where  $\nu = 2$  or  $\nu = 10$  (Figure 4 and Figure 5). All of the simulations produced a splitting thunderstorm; and further, all simulations result in similar storm development and precipitation patterns resembling that of a strong splitting thunderstorm. Figure 4 further indicates that while the precipitation pattern appears to change with different collection efficiency datasets and holding  $\nu$  constant, the total precipitation amount does not vary much. However, examining a single pair of collection efficiency dataset simulations, the total precipitation amount changes when moving from  $\nu = 2$  to  $\nu = 10$ .

The greater sensitivity to the rain shape parameter is further confirmed by Figure 5 which shows the domain mean rainfall rate ( $\text{mm min}^{-1} \text{km}^{-2}$ ) versus time (5a) and the total rainfall (kg) versus time (5b) for all  $\nu = 2$  and  $\nu = 10$  simulations. This figure demonstrates that the rain shape parameter exerts a much stronger control on the accumulated rainfall and rainfall rate than that exerted by any of the collection efficiencies investigated here. The impacts the changing collection efficiency dataset have on the precipitation processes will be examined in this section. A further examination of the changes to rainfall that occur with changing  $\nu$  will be presented in Section 4.

Although the accumulated precipitation in all collection efficiency dataset simulations remains approximately the same (with a maximum percent change reaching 10% of total accumulated

rainfall by the end of the simulation), the processes that result in the surface rainfall differ between the eight simulations. In order to examine the changes in the rain production processes, a detailed microphysical budget was prepared, showing every process within the model that creates or removes rain from the atmosphere, with the exception of precipitation to the surface. This will allow for examination of the processes that will be affected by changing collection efficiency, autoconversion and rain accretion, as well as the secondary effects cascading from changes to autoconversion and rain accretion. The detailed microphysical budget was compiled by vertically integrating each rain source and sink term and averaging them across the domain and at all times. In Figure 6, cloud collection (red dots) relates to cloud and drizzle collision-coalescence with rain and autoconversion of cloud and drizzle to rain; collision melting (orange dots) is defined as the melting of all ice species into rain through the collision of such ice species with rain; other melting (blue dots) is melting of ice into rain not including collision melting; ice accretion (green dots) is rain being accreted by ice; and condensation and evaporation (purple dots) are shown as the net of these two processes for rain only. Positive numbers indicate the creation or sources of rain, and negative numbers indicate the removal or sinks of rain. The cyan dots represent the sum of all processes.

Figure 6 indicates that while the total rain generated is more strongly controlled by the shape parameter than by the collection efficiencies (the sensitivity to shape parameter will be investigated further in Section 4), changing the collection efficiency dataset impacts the processes that lead to rain. In particular, collection efficiency dataset is the stronger control on cloud collection than the RSD width, with the Hall80 simulation producing less rain through autoconversion and cloud collection than any of the other efficiency approaches. In the following

two paragraphs, we will separate the total difference in this term into its two components: autoconversion and the collection of cloud water by falling raindrops.

The changes to the autoconversion and collection of cloud water by rain are not parsed out individually in the budget, however the changes to each of these can be inferred from examining the collection efficiency differences. Figure 2c shows that the collection efficiencies of a rain droplet of  $r = 50\mu\text{m}$  with cloud drops of  $r \leq 50\mu\text{m}$  for the Hall80, Wang09, and Pinsky01 tables are nearly the same and all lower than the Long74 dataset, which assigns all of the collection efficiencies where the collector drop has  $r \geq 50\mu\text{m}$  to unity. These lower collection efficiencies for the Hall80, Wang09, and Pinsky01 tables for rain-cloud and rain-drizzle collisions result in the lower collection of cloud mass by rain than when compared with the Long simulations for both  $v = 2$  and  $v = 10$ .

While the Long74 dataset has the most cloud-to-rain conversion, the Hall80 dataset has the least, reaching below even the Wang09 and Pinsky01 datasets. This is primarily due to a decrease in autoconversion, rather than a decrease in cloud-rain collection. This is evident by examining Figure 2d, which shows the collection efficiencies for a collector drop of  $r = 100\mu\text{m}$  and cloud and rain droplets of other sizes. For the regions of cloud and drizzle collection by rain (i.e.  $r < 50\mu\text{m}$ ), the Wang09 dataset has the same collection efficiency as the Hall80 dataset and Pinsky01 is either below (for  $r < 4\mu\text{m}$ ) or near the Hall80 dataset. This indicates that the predominant change between the Hall80 and other datasets when examining cloud collection is

due to a change in autoconversion that is brought on by a change in collection efficiencies in the cloud-cloud, cloud-drizzle, and drizzle-drizzle regions.

While the cloud collection term in the budget changes between all four efficiency tables, the total amount of precipitation generated, as well as the total amount that reaches the ground, stays approximately constant. This is due to the near-complete offsetting of reduced cloud collection and autoconversion by the reduced loss of rain to accretion by ice. This offsetting occurs due to the fact that there is less rain mass and therefore less available to be accreted by ice. Overall, while the processes that produce rain differ somewhat between the different collection efficiency tests, the shape parameter is a much stronger control on the rain processes and total rainfall amount than the collection efficiencies for these idealized deep convective simulations tests.

#### **4. Shape Parameter Results**

Figures 5 and 6 indicate that when  $\nu=10$ , the total accumulated rainfall decreases substantially when compared to  $\nu=2$ . To examine whether this is an aberration unique to the difference between the  $\nu=2$  and  $\nu=10$  simulations or a larger effect of the narrowing RSD, additional simulations were conducted with  $\nu=1, 3, 4, 6,$  and  $8$  using the Long74 Efficiency dataset (the default collection efficiency dataset in RAMS). These experiments will elucidate the effect of changing RSD width on storm processes. Like the collection efficiency experiments, changing the RSD width alone should change the liquid accretion process, but unlike the collection efficiency experiments, changing the RSD width alone will also change condensation and evaporation rates, as well as ice accretion. These processes will be examined in detail.

To examine overall precipitation differences resulting from the utilization of different shape parameters, the 5-minute running mean of the grid-averaged rainfall rate for all Long74 simulations is shown in Figure 7a and the domain total accumulated rainfall over time is shown in Figure 7b. It can be clearly seen that throughout the simulation period, the rainfall rate increases monotonically as the RSD widens (i.e., as the shape parameter decreases), producing a nearly 200% change in final accumulated rain amount across the range of shape parameters tested here. This change is offset by an increase in hail production, discussed in Section 4.3, thereby resulting in a 75% change in total accumulated precipitation. This trend of increasing rain with wider RSD is consistent with the prior observations made by Niu et al. (2009) discussed above.

Furthermore, the RSD impacts the vertical profiles of rain mass and number. It is evident that as the RSD narrows, the raindrop mass mean diameter at heights less than ~4000 m also generally decreases (Figure 7c). Above 4000 m, this trend reverses due to changes in rain self-collection (discussed in Section 4.2). A similar reversal at ~5000 m occurs in the mixing ratio, switching from narrower RSDs having larger mixing ratios above 5000m to narrower RSDs generally having smaller ratios below 5000m (Figure 7e), although the reversal is not as abrupt. Figure 7d shows that the raindrop number concentration generally increases with narrowing RSD at heights below 4500 m and decreases with narrowing RSD above that height. The RSD induced impacts on the vertical profiles of rain mass and number concentrations produce a decrease in rain rates, and therefore also in accumulated precipitation. It appears that these impacts are caused by three predominant factors: (1) a decrease in the net rain mass production, (2) a decrease in the mean

raindrop diameter and fall speed (and thus an increase of rain mixing ratio remaining in the atmosphere), and (3) changes in the ice processes as the rain RSD becomes narrower. The processes driving these factors are now examined in more detail.

#### **4.1. Change in rain mass production from evaporation**

In order to examine the changes in the rain mass production, a detailed microphysical budget was prepared as in Figure 6, showing every process within the model that creates or removes rain from the atmosphere, with the exception of precipitation to the surface. The budgets for the six Long74 simulations are shown in Figure 8a. It is evident from this figure that there is a monotonic decrease in the net rain production as the RSD narrows (as the shape parameter increases). This monotonic decrease is driven by increased evaporation (purple dots) and decreased rainfall production from collision melting (orange dots) that is not entirely offset by changes to all other melting (blue dots).

To understand why the evaporation of rain increases as the distribution narrows, it is useful to examine the condensation/evaporation equation. In this section, evaporation will be the focus, as there is more evaporation than condensation as seen in Figure 8a (indicated by the negative values for the Condensation and Evaporation term). When integrated over a gamma PDF, evaporation is proportional to  $v$  when holding number and mixing ratio constant through the following relationship:

$$\left. \frac{\partial q_r}{\partial t} \right|_{evap} \propto NM_1(S - 1) = N\bar{D}\nu \left[ \frac{\Gamma(\nu)}{\Gamma(\nu + 3)} \right]^{\frac{1}{3}} (S - 1) \quad (6)$$

where  $\left. \frac{\partial q_r}{\partial t} \right|_{evap}$  is the local time rate of change in rain mass mixing ratio due to evaporation ( $\text{kg kg}^{-1} \text{ s}^{-1}$ ),  $N$  is the number concentration of raindrops ( $\# \text{ m}^{-3}$ ),  $M_1$  is the first moment of the HSD (mm), and  $\bar{D}$  is raindrop mass mean diameter (mm) (Igel and van den Heever 2017a). According to expression (6), the evaporation rate of rain mass will increase as the first moment of the HSD increases, which partially depends on the term:  $\nu \left[ \frac{\Gamma(\nu)}{\Gamma(\nu+3)} \right]^{\frac{1}{3}}$ . Figure 8b shows the relationship between  $\nu$  and this quantity to demonstrate that it is directly dependent on  $\nu$ . The derivation of this quantity and an explanation for this dependence are presented in Appendix II.

Beyond the contribution to the increased evaporation rate directly caused by the narrowing RSD when the number and mass are held constant, there are additional factors that impact the evaporation rate, such as the actual changes to the droplet mean diameter and the number concentration. Raindrop populations comprised of a greater number of smaller raindrops are associated with enhanced evaporation rates (even though the actual magnitude of the evaporation rates are lower per droplet for smaller drops) because they fall more slowly than larger drops, thereby increasing their residence time below cloud base and their subsequent exposure to dry air. As the narrower RSDs produce a raindrop population with lower mass mean diameters below cloud base (Figure 7c), the rain within the higher  $\nu$  sensitivity tests will therefore be subjected to more evaporation because of the lower fall speeds. Furthermore, for the same liquid water content, a population comprised of more numerous smaller drops, as opposed to fewer but larger

drops, will have a larger exposed integrated surface area which will also enhance the amount of evaporation.

The changes to the evaporation result in changes in the cold pool as exhibited by changing temperatures at the surface. Figure 7f shows the maximum magnitude perturbation  $\theta_\rho$  (where perturbation is defined relative to the initial homogeneous environment) at the surface over time throughout the storm lifetime. Here, the density potential temperature  $\theta_\rho = \theta[1 + 0.61r - r_l]$  where  $r$  is the water vapor mixing ratio ( $\text{kg kg}^{-1}$ ),  $\theta$  is potential temperature (K), and  $r_l$  is the mixing ratio of liquid water in the air ( $\text{kg kg}^{-1}$ ). While Figure 7f indicates a generally colder cold pool with narrower RSD, this change does not impact the size of the cold pools substantially nor the overall storm structure.

#### **4.2. Changes in Rain Self-Collection**

Changes to collision-coalescence that result in more rain residing in the cloud will now be discussed. In broader size distributions, such as when  $\nu = 1$  or 2, the disparity in drop sizes leads to a wider range in the fall speeds of the raindrops than is found in narrower size distributions. This differential sedimentation (which is represented in RAMS in a bin-emulating fashion as described in Section 2) results in, in general, an increasing amount of rain self-collection as the RSDs widen. This can be seen in Figure 8c, which is a vertical profile of rain self-collection averaged spatially and temporally. While this trend is monotonic for all HSD widths from  $\nu = 2$  to  $\nu = 10$ , the Long74 $\nu$ 1 rain self-collection is lower than the Long74 $\nu$ 2. This is due to the increasing number of very small drops that fall at nearly the same rate in the

Long74v1 simulation when compared to the Long74v2 simulation, as is evident in Figure 1. The increased rain self-collection leads to a larger mean drop size and fewer raindrops in the broader size distribution sensitivity tests. These larger drops more readily fall out of the cloud and produce a higher instantaneous precipitation rate. Therefore, the impacts of the shape parameter on both the rain water production and the rate at which raindrops fall to the surface contribute to the decrease in the precipitation rate and accumulated precipitation with increasing  $\nu$ .

### **4.3. Change in rain mass production due to ice processes**

In addition to the increased evaporation with narrower size distributions, net rain production is also reduced through a decrease in the amount of ice melted into rain through collisions (Figure 8a). This occurs due to the changes in collision-coalescence resulting from the differences in fall speeds between rain and hail, as well as the changes in radius of rain. Rain fall speed will increase as the RSD widens, while the hail fall speed is not directly affected by the changes in RSD width. This produces many more collisions between hail and rain due to the large spread in fall speeds across the raindrop size spectrum. For narrower RSDs, more rain drops fall at similar rates and hence are less likely to collide with falling hail particles. This is reflected in the RAMS collision-coalescence equations (Walko et al. 1995). In addition to the fewer collisions that occur, as the mean raindrop radii are smaller in the narrower RSD experiments (Figure 7c), even when collisions between rain and ice do occur, the result is less likely to melt the ice, and more likely to result in the rain drop freezing onto the ice hydrometeor. This effect is accounted for in the RAMS microphysics parameterization which tracks the internal energy of hydrometeors.

While the production of rain through collision melting decreases dramatically in those simulations with narrow RSDs, there is a compensating effect in rain production through more non-contact melting (although not sufficiently more to counteract the decrease in contact melting). Increased non-contact melting is primarily caused by the larger mass fraction (compared to total hydrometeor mass) of ice in the narrower RSD cases, which results from the total cloud ice mass remaining approximately the same (Figure 9c) while the cloud liquid mass decreases with decreasing shape parameter. Along with impacting the surface rainfall, these changes in melting also have implications for hail production—especially in the higher shape parameter cases, as the increase in ice mass results in producing more hail at the surface. More accumulated hail with narrower RSD is shown in Figures 9a and 9b, which compare the spatial distribution of all ice precipitation accumulated by the end of the simulations in the Longv2 and Longv10 cases. The majority of the contribution to the increase in hail at the surface is caused by the lack of contact melting.

Figure 9d shows a spatial and temporal average vertical profile of hail (calculated over all columns containing integrated condensate  $>1 \text{ kg m}^{-2}$ ) for all of the sensitivity simulations. The figure indicates that even while the hail mass decreases below the melting layer, the fewer hail-rain collisions that occur in association with the narrower RSD results in a larger hail concentration well below the melting layer in the v10 case. While none of the simulations produce large amounts of hail at the surface, the results suggest that the amount of hail at the surface could be highly sensitive to the selection of the *a priori* rain drop shape parameter in model simulations using double-moment microphysics schemes.

## 5. Discussions and Conclusion

In this work we have examined the sensitivity of precipitation, process rates, and storm structure to changes in (1) the collection efficiencies and (2) the *a priori* assumed RSD width in three-dimensional, fully interactive idealized simulations of a deep convective storm. For the experiments where the RSD width is held constant and the collection efficiency dataset changes, the changes to the dataset used result in small changes to the overall precipitation (10%). While the total precipitation amounts do not vary strongly as a function of the different collection efficiency datasets, the precipitation processes that lead to rainfall do vary. The Hall80 efficiencies in particular produce less autoconversion than the Long74, Pinsky01, and Wang09 efficiency datasets.

For those experiments in which the collection efficiency dataset is held constant and the width of the RSD was varied using the shape parameter  $v$ , as the RSD narrows ( $v$  increases), the mean precipitation rate and total accumulated precipitation decrease (total accumulated precipitation changes up to 75% while total rainfall changes up to 200%). This occurs due to a combination of three main factors: (a) increasing evaporation that reduces rain amounts (Section 4.1), (b) slower raindrop fall speeds leading to longer residency time and changes in rain self-collection (Section 4.2), and (c) decreased rain production due to decreased ice melting (Section 4.3). Wider RSDs also result in increased hail precipitation at the surface.

Our modelling results of a decrease in precipitation with narrowing RSD are similar to the general trends evident in the limited observational results made at the ground, including those of

Niu et al. (2009). This research indicates that care should be taken when selecting a shape parameter, especially for those situations that rely on the accurate prediction of precipitation, realistic microphysical budgets and reasonable representations of cold pools. This result is especially troubling for numerical models which are expected to use a single a priori value or empirical function for the shape parameter to forecast a wide variety of convective storm types over a wide range of conditions, such as climate and forecasting models. The results presented here also indicate that changing  $\nu$  produces a wide spread in values of forecasted rainfall, and suggest that benefit may be gained in running an ensemble with varying values of  $\nu$  to improve rainfall predictions. Such an ensemble would provide the range of rainfall conditions possible due to variations in the RSD width, and could be used by forecasters to fully assess the range of predicted rainfall amounts.

The demonstrated sensitivity of rainfall to the rain shape parameter and collection efficiencies in this article suggests that more effort should be put into improving the estimate of the shape parameter rather than improving the collection kernels, and their associated collection efficiencies, for storms dominated by rain production from melting. While changing the shape parameter resulted in a much larger change to the overall precipitation than the changes to the collection efficiency datasets tested here, the collection efficiency dataset used was a much stronger control on cloud collection (including autoconversion and cloud accreted by rain) than the RSD width. This research adds to a growing body of work that indicates that improving HSD representations is one of the next big steps to improving microphysical schemes (e.g. Abel and Boutle, 2012; Shipway and Hill, 2012). Future work should be conducted with idealized studies examining more benign warm clouds and mixed-phase clouds over longer time periods in order

to understand these microphysical sensitivities in more detail. Further, future work should include case studies of convective clouds and storms while changing the shape parameter and collection efficiency datasets that include comparisons to observations to understand the complex interactions that can occur in real cases. That stated, the fact that dynamically dominant storms, such as the system simulated here, are indeed sensitive to the changes in these microphysical parameters, suggests that the impacts of these parameters could be quite significant, and need to be considered across the storm spectrum. Further, although this work was completed with only the RAMS bin-emulating microphysical scheme, the changes to rainfall amounts and process rates with changing RSD width are based in physical processes and are therefore likely to be somewhat robust within different parameterizations. However, future work should include simulations with other double-moment microphysical schemes that represent autoconversion differently (e.g., Kogan, 2013; Morrison and Milbrandt, 2015). Issues with setting the shape parameter a priori could be avoided completely with further development of microphysical parameterizations such as triple moment and bin schemes that do not rely on such specifications. However, these schemes are not as yet in wide use.

## **Acknowledgments**

*We would like to acknowledge funding from NASA Grants NNN12AA01C and 80NSSC18KD149. High-performance computing support from Yellowstone ([ark:/85065/d7wd3xhc](https://www.earth.illinois.edu/yellowstone/)) was provided by NCAR's Computational and Information Systems Laboratory, sponsored by the National Science Foundation. A. Igel and S. Freeman were supported by the National Science Foundation Graduate Research Fellowship Program under Grant No. DGE-1321845. We would like to thank Aryeh Drager for his contributions to document editing and Stephen Saleeby for his*

*helpful discussions about RAMS microphysics. We would also like to thank three anonymous reviewers whose comments led to improvements in the manuscript. The model data can be obtained by emailing the corresponding author (sean.freeman@colostate.edu).*

## **Appendix I: Description of collection efficiency dataset implementation**

None of the collection efficiency datasets were trivial to implement over all sizes in the bin-emulating component of RAMS (which range from  $r \approx 1\mu\text{m}$  to  $r \approx 6\text{mm}$ ), as the Hall80, Pinsky01, and Wang09 efficiencies are tables of discrete values that do not strictly match up to the bins in the RAMS bin-emulating scheme and the Long74 dataset has negative values below  $r \approx 5\mu\text{m}$ . For the Long74 dataset, all values for collection efficiencies below 0 were set to exactly 0. The Hall80 table contains 11 radii between  $10\mu\text{m}$  and  $300\mu\text{m}$  and 20 ratios of smaller drop radii to larger drop radii. Instead of discretizing on ratio, the Pinsky01 efficiency dataset has table values for each radius, producing a table of  $61 \times 61$  radii between  $1\mu\text{m}$  and  $250\mu\text{m}$ . To resolve the issue of non-discrete values and values that do not encompass the entire spectrum, the following steps were taken: (1) to obtain the collection efficiencies between two drops of arbitrary radius  $r_1$  and  $r_2$ , the efficiencies were linearly interpolated between the provided discrete values; (2) as the radius of the collector drop (i.e. the larger drop)  $r_1 \rightarrow 0$ ,  $E \rightarrow 0$  linearly from the smallest radius available, where  $E$  is the collection efficiency; and (3) for the Hall80 and Wang09 datasets, which use radius ratio, as  $\frac{r_2}{r_1} \rightarrow 0$ ,  $E \rightarrow 0$  linearly from the smallest  $\frac{r_2}{r_1}$  value available, where  $r_1$  is the collector drop and  $r_2$  is the collected drop. Additionally, for the Pinsky01 dataset only, as the dataset depends on pressure, the collection efficiency for an arbitrary point is linearly interpolated between the pressure values available (1000, 750, and 500

hPa). If the pressure is outside of the bounds of the given pressures, the efficiency was set to the value corresponding to the closest pressure with a value available. It should be noted that RAMS does not use these collection efficiency datasets for rain-rain collection, instead opting to use a collection efficiency of unity for all rain self collection.

## Appendix II: Description of the Evaporation Rate Relation to Shape Parameter

Evaporation rate for a gamma RSD can be expressed as follows:

$$\left. \frac{\partial q_r}{\partial t} \right|_{evap} \propto N M_1 (S - 1)$$

where  $\left. \frac{\partial q_r}{\partial t} \right|_{evap}$  is the local time rate of change in rain mass mixing ratio due to evaporation ( $\text{kg kg}^{-1} \text{ s}^{-1}$ ),  $N$  is the number concentration of raindrops ( $\# \text{ m}^{-3}$ ),  $M_1$  is the first moment of the HSD (mm), and  $\bar{D}$  is raindrop mass mean diameter (mm) (Igel and van den Heever 2017a).

For any moment  $I$ , the moment is given as:

$$M_I = \frac{\int_{-\infty}^{\infty} D^I f(D) dD}{\int_{-\infty}^{\infty} f(D) dD}$$

where  $M_I$  is the  $I^{\text{th}}$  moment,  $D$  is diameter, and  $f(D)$  is the size distribution function. Inserting  $M_1$  into the evaporation relationship results in the following:

$$\left. \frac{\partial q_r}{\partial t} \right|_{evap} \propto N \frac{\int_{-\infty}^{\infty} D^1 f(D) dD}{\int_{-\infty}^{\infty} f(D) dD} (S - 1)$$

Now, inserting the gamma HSD function in this relationship gives the following:

$$\left. \frac{\partial q_r}{\partial t} \right|_{evap} \propto N \frac{\int_{-\infty}^{\infty} D \frac{\lambda^\nu}{\Gamma(\nu)} D^{\nu-1} e^{-\lambda D} dD}{\int_{-\infty}^{\infty} \frac{\lambda^\nu}{\Gamma(\nu)} D^{\nu-1} e^{-\lambda D} dD} (S - 1)$$

Using the relationship that:

$$\bar{D}^3 = \frac{1}{\lambda^3} \left( \frac{\Gamma(\nu + 3)}{\Gamma(\nu)} \right); \bar{D} = \frac{1}{\lambda} \left( \frac{\Gamma(\nu + 3)}{\Gamma(\nu)} \right)^{1/3}; \lambda = \frac{1}{\bar{D}} \left( \frac{\Gamma(\nu + 3)}{\Gamma(\nu)} \right)^{1/3}$$

where  $\bar{D}$  is the mass mean diameter. Integrating this equation we obtain :

$$\left. \frac{\partial q_r}{\partial t} \right|_{evap} \propto N \bar{D} \nu \left( \frac{\Gamma(\nu + 3)}{\Gamma(\nu)} \right)^{-1/3} (S - 1)$$

The reasons for the dependence of the first moment of the HSD on  $\nu$  are not necessarily intuitive.

To understand why the first moment (proportional to the integrated diameter) increases with increasing  $\nu$  when holding mass and number constant, it is helpful to consider the more general physical question of whether any moment  $I$  is increased or decreased due to a change in shape parameter when number and mass (zeroth and third moment, respectively) are held constant.

Very high moments will increase as  $\nu$  decreases (that is as the HSD becomes broader). This is because for small  $\nu$  there are more very large drops than there are for large  $\nu$  (see Figure 1). This means, for example, that the 1000<sup>th</sup> moment will depend primarily on only the large drops as a moment  $I$  is proportional to the integration of  $D^I$  over all diameters, and  $D_{small}^{1000} \ll D_{large}^{1000}$ . For

lower and lower moments, the relative number of drops in the centre and left tail of the distribution (where smaller drops reside) begin to have a greater impact in determining whether a moment increases or decreases with  $v$  until eventually, they matter equally as much as the relative number in the right tail, when calculating the third moment. The third moment is held constant by design and does not depend on  $v$ . For the first and second moments, the centre of the distribution, where more drops reside in HSDs with higher  $v$ , becomes the most important. Therefore, these moments must increase for higher  $v$  when the number and mass are specified to be constant.

## References

- Abel, S. J., and I. A. Boutle, 2012: An improved representation of the raindrop size distribution for single-moment microphysics schemes. *Q. J. R. Meteorol. Soc.*, **138**, 2151–2162, doi:10.1002/qj.1949. <http://doi.wiley.com/10.1002/qj.1949> (Accessed January 10, 2019).
- Adams-Selin, R. D., S. C. van den Heever, and R. H. Johnson, 2012: Impact of Graupel Parameterization Schemes on Idealized Bow Echo Simulations. *Mon. Weather Rev.*, **141**, 1241–1262, doi:10.1175/MWR-D-12-00064.1. <https://doi.org/10.1175/MWR-D-12-00064.1>.
- Adirosi, E., L. Baldini, F. Lombardo, F. Russo, F. Napolitano, E. Volpi, and A. Tokay, 2015: Comparison of different fittings of drop spectra for rainfall retrievals. *Adv. Water Resour.*, **83**, 55–67, doi:10.1016/j.advwatres.2015.05.009. <http://www.sciencedirect.com/science/article/pii/S0309170815001025> (Accessed December 9, 2015).
- , E. Volpi, F. Lombardo, and L. Baldini, 2016: Raindrop size distribution: Fitting performance of common theoretical models. *Adv. Water Resour.*, **96**, 290–305, doi:10.1016/j.advwatres.2016.07.010.
- Alexander, C., and Coauthors, 2016: The hourly updated US High-Resolution Rapid Refresh (HRRR) storm-scale forecast model. *Geophys. Res. Abst.*, **18**.
- Ayala, O., B. Rosa, and L.-P. Wang, 2008: Effects of turbulence on the geometric collision rate of sedimenting droplets. Part 2. Theory and parameterization. *New J. Phys.*, **10**, 075016, doi:10.1088/1367-2630/10/7/075016. <http://stacks.iop.org/1367->

2630/10/i=7/a=075016?key=crossref.4f55f255acdc462fae87c0d8e24d2917.

Barth, M. C., and Coauthors, 2007: Cloud-scale model intercomparison of chemical constituent transport in deep convection. *Atmos. Chem. Phys.*, **7**, 4709–4731, doi:10.5194/acp-7-4709-2007. <http://www.atmos-chem-phys.net/7/4709/2007/>.

Barthlott, C., B. Mühr, and C. Hoose, 2017: Sensitivity of the 2014 Pentecost storms over Germany to different model grids and microphysics schemes. *Q. J. R. Meteorol. Soc.*, **143**, 1485–1503, doi:10.1002/qj.3019. <https://doi.org/10.1002/qj.3019>.

Beard, K. V., and H. T. Ochs, 1984: Collection and coalescence efficiencies for accretion. *J. Geophys. Res.*, **89**, 7165, doi:10.1029/JD089iD05p07165. <http://doi.wiley.com/10.1029/JD089iD05p07165> (Accessed May 31, 2018).

Benmoshe, N., M. Pinsky, A. Pokrovsky, and A. Khain, 2012: Turbulent effects on the microphysics and initiation of warm rain in deep convective clouds: 2-D simulations by a spectral mixed-phase microphysics cloud model. *J. Geophys. Res. Atmos.*, **117**, n/a-n/a, doi:10.1029/2011JD016603. <http://doi.wiley.com/10.1029/2011JD016603> (Accessed December 19, 2018).

Bringi, V. N., C. R. Williams, M. Thurai, and P. T. May, 2009: Using Dual-Polarized Radar and Dual-Frequency Profiler for DSD Characterization: A Case Study from Darwin, Australia. *J. Atmos. Ocean. Technol.*, **26**, 2107–2122, doi:10.1175/2009JTECHA1258.1. <http://dx.doi.org/10.1175/2009JTECHA1258.1>.

Brown, B. R., M. M. Bell, and A. J. Frambach, 2016: Validation of simulated hurricane drop size distributions using polarimetric radar. *Geophys. Res. Lett.*, **43**, 910–917, doi:10.1002/2015GL067278. <http://doi.wiley.com/10.1002/2015GL067278> .

- Bryan, G. H., and H. Morrison, 2012: Sensitivity of a Simulated Squall Line to Horizontal Resolution and Parameterization of Microphysics. *Mon. Weather Rev.*, **140**, 202–225, doi:10.1175/MWR-D-11-00046.1. <http://journals.ametsoc.org/doi/abs/10.1175/MWR-D-11-00046.1> .
- Cao, Q., G. Zhang, E. Brandes, T. Schuur, A. Ryzhkov, and K. Ikeda, 2008: Analysis of Video Disdrometer and Polarimetric Radar Data to Characterize Rain Microphysics in Oklahoma. *J. Appl. Meteorol. Climatol.*, **47**, 2238–2255, doi:10.1175/2008JAMC1732.1. <http://dx.doi.org/10.1175/2008JAMC1732.1>.
- Chen, S., M. K. Yau, P. Bartello, S. Chen, M. K. Yau, and P. Bartello, 2018: Turbulence Effects of Collision Efficiency and Broadening of Droplet Size Distribution in Cumulus Clouds. *J. Atmos. Sci.*, **75**, 203–217, doi:10.1175/JAS-D-17-0123.1. <http://journals.ametsoc.org/doi/10.1175/JAS-D-17-0123.1> .
- Cohard, J.-M., and J.-P. Pinty, 2000: A comprehensive two-moment warm microphysical bulk scheme. I: Description and tests. *Q. J. R. Meteorol. Soc.*, **126**, 1815–1842, doi:10.1002/qj.49712656613. <http://doi.wiley.com/10.1002/qj.49712656613> .
- Cohen, C., and E. W. McCaul, 2006: The Sensitivity of Simulated Convective Storms to Variations in Prescribed Single-Moment Microphysics Parameters that Describe Particle Distributions, Sizes, and Numbers. *Mon. Weather Rev.*, **134**, 2547–2565, doi:10.1175/MWR3195.1. <http://dx.doi.org/10.1175/MWR3195.1>.
- Cotton, W. R., and Coauthors, 2003a: RAMS 2001: Current status and future directions. *Meteorol. Atmos. Phys.*, **82**, 5–29, doi:10.1007/s00703-001-0584-9. <http://www.springerlink.com/Index/10.1007/s00703-001-0584-9>.

Cotton, W. R., and Coauthors, 2003b: RAMS 2001: Current status and future directions.

*Meteorol. Atmos. Phys.*, **82**, 5–29, doi:10.1007/s00703-001-0584-9.

<http://193.144.100.163/meteorologia/DOCS/BIBLIOGRAFIA/METATMPHYS-cottonrams.pdf>.

Ćurić, M., D. Janc, and K. Veljović, 2010: Dependence of accumulated precipitation on cloud drop size distribution. *Theor. Appl. Climatol.*, **102**, 471–481, doi:10.1007/s00704-010-0332-5. <http://dx.doi.org/10.1007/s00704-010-0332-5>.

Davis, M. H., 1972: Collisions of Small Cloud Droplets: Gas Kinetic Effects. *J. Atmos. Sci.*, **29**, 911–915, doi:10.1175/1520-0469(1972)029<0911:COSSCDG>2.0.CO;2. [https://doi.org/10.1175/1520-0469\(1972\)029%3C0911:COSSCDG%3E2.0.CO](https://doi.org/10.1175/1520-0469(1972)029%3C0911:COSSCDG%3E2.0.CO).

Federico, S., E. Avolio, M. Petracca, G. Panegrossi, P. Sanò, D. Casella, and S. Dietrich, 2014: Simulating lightning into the RAMS model: implementation and preliminary results. *Nat. Hazards Earth Syst. Sci.*, **14**, 2933–2950, doi:10.5194/nhess-14-2933-2014. <http://www.nat-hazards-earth-syst-sci.net/14/2933/2014/>.

Feingold, G., R. L. Walko, B. Stevens, and W. R. Cotton, 1998: Simulations of marine stratocumulus using a new microphysical parameterization scheme. *Atmos. Res.*, **47–48**, 505–528, doi:10.1016/S0169-8095(98)00058-1. <https://www.sciencedirect.com/science/article/pii/S0169809598000581> .

Freud, E., D. Rosenfeld, M. O. Andreae, A. A. Costa, and P. Artaxo, 2008: Robust relations between CCN and the vertical evolution of cloud drop size distribution in deep convective clouds. *Atmos. Chem. Phys.*, **8**, 1661–1675, doi:10.5194/acp-8-1661-2008. <http://www.atmos-chem-phys.net/8/1661/2008/>.

- Friedrich, K., E. a. Kalina, J. Aikins, M. Steiner, D. Gochis, P. a. Kucera, K. Ikeda, and J. Sun, 2015: Raindrop size distribution and rain characteristics during the 2013 Great Colorado Flood. *J. Hydrometeorol.*, 150526130654002, doi:10.1175/JHM-D-14-0184.1.  
<http://journals.ametsoc.org/doi/abs/10.1175/JHM-D-14-0184.1>.
- Gaudet, B. J., and W. R. Cotton, 2006: Low-Level Mesocyclonic Concentration by Nonaxisymmetric Transport. Part I: Supercell and Mesocyclone Evolution. *J. Atmos. Sci.*, **63**, 1113–1133, doi:10.1175/JAS3685.1. <http://dx.doi.org/10.1175/JAS3685.1>.
- , ———, and M. T. Montgomery, 2006: Low-Level Mesocyclonic Concentration by Nonaxisymmetric Transport. Part II: Vorticity Dynamics. *J. Atmos. Sci.*, **63**, 1134–1150, doi:10.1175/JAS3579.1. <http://dx.doi.org/10.1175/JAS3579.1>.
- Gilmore, M. S., J. M. Straka, and E. N. Rasmussen, 2004: Precipitation Uncertainty Due to Variations in Precipitation Particle Parameters within a Simple Microphysics Scheme. *Mon. Weather Rev.*, **132**, 2610–2627, doi:10.1175/MWR2810.1.  
<http://dx.doi.org/10.1175/MWR2810.1>.
- Gonçalves, F. L. T., J. A. Martins, and M. A. Silva Dias, 2008: Shape parameter analysis using cloud spectra and gamma functions in the numerical modeling RAMS during LBA Project at Amazonian region, Brazil. *Atmos. Res.*, **89**, 1–11, doi:10.1016/j.atmosres.2007.12.005.
- Grant, L. D., and S. C. van den Heever, 2014: Microphysical and Dynamical Characteristics of Low-Precipitation and Classic Supercells. *J. Atmos. Sci.*, **71**, 2604–2624, doi:10.1175/JAS-D-13-0261.1. <http://dx.doi.org/10.1175/JAS-D-13-0261.1>.
- Grasso, L. D., 2000: The Dissipation of a Left-Moving Cell in a Severe Storm Environment. *Mon. Weather Rev.*, **128**, 2797–2815, doi:10.1175/1520-

0493(2000)128<2797:TDOALM>2.0.CO;2. [http://dx.doi.org/10.1175/1520-0493\(2000\)128%3C2797:TDOALM%3E2.0.CO](http://dx.doi.org/10.1175/1520-0493(2000)128%3C2797:TDOALM%3E2.0.CO).

Grubišić, V., R. K. Vellore, and A. W. Huggins, 2005: Quantitative Precipitation Forecasting of Wintertime Storms in the Sierra Nevada: Sensitivity to the Microphysical Parameterization and Horizontal Resolution. *Mon. Weather Rev.*, **133**, 2834–2859, doi:10.1175/MWR3004.1. <http://journals.ametsoc.org/doi/abs/10.1175/MWR3004.1> .

Hall, W. D., 1980: A Detailed Microphysical Model Within a Two-Dimensional Dynamic Framework: Model Description and Preliminary Results. *J. Atmos. Sci.*, **37**, 2486–2507, doi:10.1175/1520-0469(1980)037<2486:ADMMWA>2.0.CO;2. [https://doi.org/10.1175/1520-0469\(1980\)037%253C2486:ADMMWA%253E2.0.CO](https://doi.org/10.1175/1520-0469(1980)037%253C2486:ADMMWA%253E2.0.CO).

van den Heever, S. C., and W. R. Cotton, 2004: The impact of hail size on simulated supercell storms. *J. Atmos. Sci.*, **61**, 1596–1609.

Heymsfield, A. J., A. Bansemer, M. R. Poellot, and N. Wood, 2015: Observations of Ice Microphysics through the Melting Layer. *J. Atmos. Sci.*, **72**, 2902–2928, doi:10.1175/JAS-D-14-0363.1. <http://dx.doi.org/10.1175/JAS-D-14-0363.1>.

Hsieh, W. C., H. Jonsson, L.-P. Wang, R. C. Flagan, J. H. Seinfeld, A. Nenes, and G. Buzorius, 2009: On the representation of droplet coalescence and autoconversion: Evaluation using ambient cloud droplet size distributions. <https://calhoun.nps.edu/handle/10945/42257>.

Igel, A. L., and S. C. van den Heever, 2017a: The Importance of the Shape of Cloud Droplet Size Distributions in Shallow Cumulus Clouds. Part I: Bin Microphysics Simulations. *J. Atmos. Sci.*, **74**, 249–258, doi:10.1175/JAS-D-15-0382.1. <http://dx.doi.org/10.1175/JAS-D-15-0382.1>.

- , and ——, 2017b: The importance of the cloud droplet size distributions in shallow cumulus clouds. Part II: Macrophysical and optical properties. *J. Atmos. Sci.*, 259–273, doi:10.1175/JAS-D-15-0383.1.
- , M. R. Igel, and S. C. van den Heever, 2014: Make It a Double? Sobering Results from Simulations Using Single-Moment Microphysics Schemes. *J. Atmos. Sci.*, **72**, 910–925, doi:10.1175/JAS-D-14-0107.1. <http://dx.doi.org/10.1175/JAS-D-14-0107.1>.
- Jonas, P. R., 1972: The collision efficiency of small drops. *Q. J. R. Meteorol. Soc.*, **98**, 681–683, doi:10.1002/qj.49709841717. <https://doi.org/10.1002/qj.49709841717>.
- Kessler, E., 1969: On the Distribution and Continuity of Water Substance in Atmospheric Circulations BT - On the Distribution and Continuity of Water Substance in Atmospheric Circulations. E. Kessler, Ed., American Meteorological Society, Boston, MA, 1–84 [https://doi.org/10.1007/978-1-935704-36-2\\_1](https://doi.org/10.1007/978-1-935704-36-2_1).
- Khain, A. P., and Coauthors, 2015: Representation of microphysical processes in cloud-resolving models: Spectral (bin) microphysics versus bulk parameterization. *Rev. Geophys.*, **53**, 247–322, doi:10.1002/2014RG000468. <http://doi.wiley.com/10.1002/2014RG000468> .
- Khairoutdinov, M., and Y. Kogan, 2000: A New Cloud Physics Parameterization in a Large-Eddy Simulation Model of Marine Stratocumulus. *Mon. Weather Rev.*, **128**, 229–243, doi:10.1175/1520-0493(2000)128<0229:ANCPPI>2.0.CO;2. <http://journals.ametsoc.org/doi/abs/10.1175/1520-0493%282000%29128%3C0229%3AANCPPI%3E2.0.CO%3B2> .
- Kinzer, G. D., and W. E. Cobb, 1958: Laboratory Measurements and Analysis of the Growth and Collection Efficiency of Cloud Droplets. *J. Meteorol.*, **15**, 138–148, doi:10.1175/1520-

0469(1958)015<0138:LMAAOT>2.0.CO;2.

<http://journals.ametsoc.org/doi/abs/10.1175/1520->

0469%281958%29015%3C0138%3ALMAAOT%3E2.0.CO%3B2 .

Klett, J. D., and M. H. Davis, 1973: Theoretical Collision Efficiencies of Cloud Droplets at

Small Reynolds Numbers. *J. Atmos. Sci.*, **30**, 107–117, doi:10.1175/1520-

0469(1973)030<0107:TCEOCD>2.0.CO;2. <https://doi.org/10.1175/1520->

0469(1973)030%3C0107:TCEOCD%3E2.0.CO.

Kogan, Y., 2013: A Cumulus Cloud Microphysics Parameterization for Cloud-Resolving

Models. *J. Atmos. Sci.*, **70**, 1423–1436, doi:10.1175/JAS-D-12-0183.1.

<http://journals.ametsoc.org/doi/abs/10.1175/JAS-D-12-0183.1> .

Lang, S. E., and Coauthors, 2014: Benefits of a Fourth Ice Class in the Simulated Radar

Reflectivities of Convective Systems Using a Bulk Microphysics Scheme. *J. Atmos. Sci.*,

**71**, 3583–3612, doi:10.1175/JAS-D-13-0330.1.

<http://journals.ametsoc.org/doi/abs/10.1175/JAS-D-13-0330.1> .

Lebo, Z. J., and J. H. Seinfeld, 2011: Theoretical basis for convective invigoration due to

increased aerosol concentration. *Atmos. Chem. Phys.*, **11**, 5407–5429, doi:10.5194/acp-11-

5407-2011. <http://www.atmos-chem-phys.net/11/5407/2011/>.

Lee, H., and J.-J. Baik, 2016: Effects of turbulence-induced collision enhancement on heavy

precipitation: The 21 September 2010 case over the Korean Peninsula. *J. Geophys. Res.*

*Atmos.*, **121**, 12,319–12,342, doi:10.1002/2016JD025168.

<http://doi.wiley.com/10.1002/2016JD025168> .

Lerach, D. G., B. J. Gaudet, and W. R. Cotton, 2008: Idealized simulations of aerosol influences

on tornadogenesis. *Geophys. Res. Lett.*, **35**, n/a-n/a, doi:10.1029/2008GL035617.

<http://dx.doi.org/10.1029/2008GL035617>.

Lin, C. L., and S. C. Lee, 1975: Collision Efficiency of Water Drops in the Atmosphere. *J. Atmos. Sci.*, **32**, 1412–1418, doi:10.1175/1520-0469(1975)032<1412:CEOWDI>2.0.CO;2.

[https://doi.org/10.1175/1520-0469\(1975\)032%3C1412:CEOWDI%3E2.0.CO](https://doi.org/10.1175/1520-0469(1975)032%3C1412:CEOWDI%3E2.0.CO).

Liu, Y., and P. H. Daum, 2004: Parameterization of the Autoconversion Process. Part I: Analytical Formulation of the Kessler-Type Parameterizations. *J. Atmos. Sci.*, **61**, 1539–1548, doi:10.1175/1520-0469(2004)061<1539:POTAPI>2.0.CO;2.

[http://journals.ametsoc.org/doi/abs/10.1175/1520-](http://journals.ametsoc.org/doi/abs/10.1175/1520-0469%282004%29061%3C1539%3APOTAPI%3E2.0.CO%3B2)

[0469%282004%29061%3C1539%3APOTAPI%3E2.0.CO%3B2](http://journals.ametsoc.org/doi/abs/10.1175/1520-0469%282004%29061%3C1539%3APOTAPI%3E2.0.CO%3B2) .

Loftus, A. M., D. B. Weber, and C. A. Doswell, 2008: Parameterized Mesoscale Forcing Mechanisms for Initiating Numerically Simulated Isolated Multicellular Convection. *Mon. Weather Rev.*, **136**, 2408–2421, doi:10.1175/2007MWR2133.1.

<http://dx.doi.org/10.1175/2007MWR2133.1>.

Loftus, A. M., W. R. Cotton, and G. G. Carrió, 2014: A triple-moment hail bulk microphysics scheme. Part I: Description and initial evaluation. *Atmos. Res.*, **149**, 35–57, doi:10.1016/j.atmosres.2014.05.013.

<http://www.sciencedirect.com/science/article/pii/S0169809514002142> .

Long, A. B., 1974: Solutions to the Droplet Collection Equation for Polynomial Kernels. *J. Atmos. Sci.*, **31**, 1040–1052, doi:10.1175/1520-0469(1974)031<1040:STTDCE>2.0.CO;2.

[https://doi.org/10.1175/1520-0469\(1974\)031%253C1040:STTDCE%253E2.0.CO](https://doi.org/10.1175/1520-0469(1974)031%253C1040:STTDCE%253E2.0.CO).

Marshall, J. S., and W. M. K. Palmer, 1948: THE DISTRIBUTION OF RAINDROPS WITH

SIZE. *J. Meteorol.*, **5**, 165–166, doi:10.1175/1520-0469(1948)005<0165:TDORWS>2.0.CO;2. [http://dx.doi.org/10.1175/1520-0469\(1948\)005%3C0165:TDORWS%3E2.0.CO](http://dx.doi.org/10.1175/1520-0469(1948)005%3C0165:TDORWS%3E2.0.CO).

Meyers, M. P., R. L. Walko, J. Y. Harrington, and W. R. Cotton, 1997: New RAMS cloud microphysics parameterization. Part II: The two-moment scheme. *Atmos. Res.*, **45**, 3–39, doi:10.1016/S0169-8095(97)00018-5.

<http://linkinghub.elsevier.com/retrieve/pii/S0169809597000185> .

Milbrandt, J. A., and M. K. Yau, 2005a: A Multimoment Bulk Microphysics Parameterization. Part II: A Proposed Three-Moment Closure and Scheme Description. *J. Atmos. Sci.*, **62**, 3065–3081, doi:10.1175/JAS3535.1. <http://dx.doi.org/10.1175/JAS3535.1>.

———, and ———, 2005b: A Multimoment Bulk Microphysics Parameterization. Part I: Analysis of the Role of the Spectral Shape Parameter. *J. Atmos. Sci.*, **62**, 3051–3064, doi:10.1175/JAS3534.1. <http://dx.doi.org/10.1175/JAS3534.1>.

———, and ———, 2006: A Multimoment Bulk Microphysics Parameterization. Part IV: Sensitivity Experiments. *J. Atmos. Sci.*, **63**, 3137–3159, doi:10.1175/JAS3817.1. <http://dx.doi.org/10.1175/JAS3817.1>.

———, and R. McTaggart-Cowan, 2010: Sedimentation-Induced Errors in Bulk Microphysics Schemes. *J. Atmos. Sci.*, **67**, 3931–3948, doi:10.1175/2010JAS3541.1. <https://doi.org/10.1175/2010JAS3541.1>.

Milbrandt, J. A., S. Bélair, M. Faucher, M. Vallée, M. L. Carrera, and A. Glazer, 2016: The Pan-Canadian High Resolution (2.5 km) Deterministic Prediction System. *Weather Forecast.*, **31**, 1791–1816, doi:10.1175/WAF-D-16-0035.1. <https://doi.org/10.1175/WAF-D-16-0035.1>.

0035.1.

Mitchell, D. L., 1996: Use of Mass- and Area-Dimensional Power Laws for Determining Precipitation Particle Terminal Velocities. *J. Atmos. Sci.*, **53**, 1710–1723, doi:10.1175/1520-0469(1996)053<1710:UOMAAD>2.0.CO;2.  
<http://journals.ametsoc.org/doi/abs/10.1175/1520-0469%281996%29053%3C1710%3AUOMAAD%3E2.0.CO%3B2> .

Morrison, H., and A. Gettelman, 2008: A New Two-Moment Bulk Stratiform Cloud Microphysics Scheme in the Community Atmosphere Model, Version 3 (CAM3). Part I: Description and Numerical Tests. *J. Clim.*, **21**, 3642–3659, doi:10.1175/2008JCLI2105.1.  
<http://journals.ametsoc.org/doi/abs/10.1175/2008JCLI2105.1> .

———, and J. Milbrandt, 2010: Comparison of Two-Moment Bulk Microphysics Schemes in Idealized Supercell Thunderstorm Simulations. *Mon. Weather Rev.*, **139**, 1103–1130, doi:10.1175/2010MWR3433.1. <http://dx.doi.org/10.1175/2010MWR3433.1>.

———, and J. A. Milbrandt, 2015: Parameterization of Cloud Microphysics Based on the Prediction of Bulk Ice Particle Properties. Part I: Scheme Description and Idealized Tests. *J. Atmos. Sci.*, **72**, 287–311, doi:10.1175/JAS-D-14-0065.1.  
<http://journals.ametsoc.org/doi/10.1175/JAS-D-14-0065.1> .

———, W. W. Grabowski, H. Morrison, and W. W. Grabowski, 2007: Comparison of Bulk and Bin Warm-Rain Microphysics Models Using a Kinematic Framework. *J. Atmos. Sci.*, **64**, 2839–2861, doi:10.1175/JAS3980. <http://journals.ametsoc.org/doi/abs/10.1175/JAS3980> .

Morrison, H., G. Thompson, and V. Tatarskii, 2009: Impact of Cloud Microphysics on the Development of Trailing Stratiform Precipitation in a Simulated Squall Line: Comparison

of One- and Two-Moment Schemes. *Mon. Weather Rev.*, **137**, 991–1007,  
doi:10.1175/2008MWR2556.1. <http://dx.doi.org/10.1175/2008MWR2556.1>.

Nair, U. S., Y. Wu, C. D. Holmes, A. Ter Schure, G. Kallos, and J. T. Walters, 2013: Cloud-resolving simulations of mercury scavenging and deposition in thunderstorms. *Atmos. Chem. Phys.*, **13**, 10143–10157, doi:10.5194/acp-13-10143-2013. <http://www.atmos-chem-phys.net/13/10143/2013/>.

Naumann, A. K., and A. Seifert, 2016: Evolution of the Shape of the Raindrop Size Distribution in Simulated Shallow Cumulus. *J. Atmos. Sci.*, **73**, 2279–2297, doi:10.1175/JAS-D-15-0263.1. <https://doi.org/10.1175/JAS-D-15-0263.1>.

Niu, S., X. Jia, J. Sang, X. Liu, C. Lu, and Y. Liu, 2009: Distributions of Raindrop Sizes and Fall Velocities in a Semiarid Plateau Climate: Convective versus Stratiform Rains. *J. Appl. Meteorol. Climatol.*, **49**, 632–645, doi:10.1175/2009JAMC2208.1. <http://dx.doi.org/10.1175/2009JAMC2208.1>.

Ovtchinnikov, M., and Y. L. Kogan, 2000: An Investigation of Ice Production Mechanisms in Small Cumuliform Clouds Using a 3D Model with Explicit Microphysics. Part I: Model Description. *J. Atmos. Sci.*, **57**, 2989–3003, doi:10.1175/1520-0469(2000)057<2989:AIOIPM>2.0.CO;2. [http://dx.doi.org/10.1175/1520-0469\(2000\)057%3C2989:AIOIPM%3E2.0.CO](http://dx.doi.org/10.1175/1520-0469(2000)057%3C2989:AIOIPM%3E2.0.CO).

Pinsky, M., A. Khain, M. Shapiro, M. Pinsky, A. Khain, and M. Shapiro, 1999: Collisions of Small Drops in a Turbulent Flow. Part I: Collision Efficiency. Problem Formulation and Preliminary Results. *J. Atmos. Sci.*, **56**, 2585–2600, doi:10.1175/1520-0469(1999)056<2585:COSDIA>2.0.CO;2.

<http://journals.ametsoc.org/doi/abs/10.1175/1520-0469%281999%29056%3C2585%3ACOSDIA%3E2.0.CO%3B2> .

Pinsky, M., A. Khain, and M. Shapiro, 2001: Collision Efficiency of Drops in a Wide Range of Reynolds Numbers: Effects of Pressure on Spectrum Evolution. *J. Atmos. Sci.*, **58**, 742–764, doi:10.1175/1520-0469(2001)058<0742:CEODIA>2.0.CO;2. [https://doi.org/10.1175/1520-0469\(2001\)058%3C0742:CEODIA%3E2.0.CO](https://doi.org/10.1175/1520-0469(2001)058%3C0742:CEODIA%3E2.0.CO).

Posselt, R., and U. Lohmann, 2009: Sensitivity of the total anthropogenic aerosol effect to the treatment of rain in a global climate model. *Geophys. Res. Lett.*, **36**, n/a-n/a, doi:10.1029/2008GL035796. <http://doi.wiley.com/10.1029/2008GL035796> .

Rasmussen, R. M., I. Geresdi, G. Thompson, K. Manning, and E. Karplus, 2002: Freezing Drizzle Formation in Stably Stratified Layer Clouds: The Role of Radiative Cooling of Cloud Droplets, Cloud Condensation Nuclei, and Ice Initiation. *J. Atmos. Sci.*, **59**, 837–860, doi:10.1175/1520-0469(2002)059<0837:FDFISS>2.0.CO;2. [http://dx.doi.org/10.1175/1520-0469\(2002\)059%3C0837:FDFISS%3E2.0.CO](http://dx.doi.org/10.1175/1520-0469(2002)059%3C0837:FDFISS%3E2.0.CO).

Rogers, E., T. Black, B. Ferrier, Y. Lin, D. Parrish, and G. DiMego, 2002: Changes to the NCEP Meso Eta Analysis and Forecast System: Increase in resolution, new cloud microphysics, modified precipitation assimilation, modified 3DVAR analysis. <http://www.emc.ncep.noaa.gov/mmb/mmbpll/eta12tpb/>.

Saleeby, S. M., and W. R. Cotton, 2004: A Large-Droplet Mode and Prognostic Number Concentration of Cloud Droplets in the Colorado State University Regional Atmospheric Modeling System (RAMS). Part I: Module Descriptions and Supercell Test Simulations. *J. Appl. Meteorol.*, **43**, 182–195, doi:10.1175/1520-

0450(2004)043<0182:ALMAPN>2.0.CO;2. [http://dx.doi.org/10.1175/1520-0450\(2004\)043%3C0182:ALMAPN%3E2.0.CO](http://dx.doi.org/10.1175/1520-0450(2004)043%3C0182:ALMAPN%3E2.0.CO).

——, and ——, 2008: A Binned Approach to Cloud-Droplet Riming Implemented in a Bulk Microphysics Model. *J. Appl. Meteorol. Climatol.*, **47**, 694–703, doi:10.1175/2007JAMC1664.1. <http://dx.doi.org/10.1175/2007JAMC1664.1>.

——, and S. C. van den Heever, 2013: Developments in the CSU-RAMS Aerosol Model: Emissions, Nucleation, Regeneration, Deposition, and Radiation. *J. Appl. Meteorol. Climatol.*, **52**, 2601–2622, doi:10.1175/JAMC-D-12-0312.1. <http://dx.doi.org/10.1175/JAMC-D-12-0312.1>.

Schlamp, R. J., S. N. Grover, H. R. Pruppacher, and A. E. Hamielec, 1976: A Numerical Investigation of the Effect of Electric Charges and Vertical External Electric Fields on the Collision Efficiency of Cloud Drops. *J. Atmos. Sci.*, **33**, 1747–1755, doi:10.1175/1520-0469(1976)033<1747:ANIOTE>2.0.CO;2. [https://doi.org/10.1175/1520-0469\(1976\)033%3C1747:ANIOTE%3E2.0.CO](https://doi.org/10.1175/1520-0469(1976)033%3C1747:ANIOTE%3E2.0.CO).

Schumacher, R. S., 2009: Mechanisms for Quasi-Stationary Behavior in Simulated Heavy-Rain-Producing Convective Systems. *J. Atmos. Sci.*, **66**, 1543–1568, doi:10.1175/2008JAS2856.1. <http://dx.doi.org/10.1175/2008JAS2856.1>.

Seifert, A., 2008: On the Parameterization of Evaporation of Raindrops as Simulated by a One-Dimensional Rainshaft Model. *J. Atmos. Sci.*, **65**, 3608–3619, doi:10.1175/2008JAS2586.1. <https://doi.org/10.1175/2008JAS2586.1>.

——, and K. D. Beheng, 2001: A double-moment parameterization for simulating autoconversion, accretion and selfcollection. *Atmos. Res.*, **59–60**, 265–281,

doi:10.1016/S0169-8095(01)00126-0.

<https://www.sciencedirect.com/science/article/pii/S0169809501001260> .

Shafir, U., and T. Gal-Chen, 1971: A Numerical Study of Collision Efficiencies and Coalescence Parameters for Droplet Pairs with Radii up to 300 Microns. *J. Atmos. Sci.*, **28**, 741–751, doi:10.1175/1520-0469(1971)028<0741:ANSOCE>2.0.CO;2.  
[https://doi.org/10.1175/1520-0469\(1971\)028%3C0741:ANSOCE%3E2.0.CO](https://doi.org/10.1175/1520-0469(1971)028%3C0741:ANSOCE%3E2.0.CO).

Shipway, B. J., and A. A. Hill, 2012: Diagnosis of systematic differences between multiple parametrizations of warm rain microphysics using a kinematic framework. *Q. J. R. Meteorol. Soc.*, **138**, 2196–2211, doi:10.1002/qj.1913. <http://doi.wiley.com/10.1002/qj.1913> .

Smagorinsky, J., 1963: General Circulation Experiments with the Primitive Equations: I. The Basic Experiment. *Mon. Weather Rev.*, **91**, 99–164, doi:10.1175/1520-0493(1963)091<0099:GCEWTP>2.3.CO;2.  
<http://journals.ametsoc.org/doi/abs/10.1175/1520-0493%281963%29091%3C0099%3AGCEWTP%3E2.3.CO%3B2> .

Snook, N., and M. Xue, 2008: Effects of microphysical drop size distribution on tornadogenesis in supercell thunderstorms. *Geophys. Res. Lett.*, **35**, L24803, doi:10.1029/2008GL035866. <http://doi.wiley.com/10.1029/2008GL035866> .

Takuro, M., and T. Toshihiko, 2015: Evaluation of autoconversion schemes in a single model framework with satellite observations. *J. Geophys. Res. Atmos.*, **120**, 9570–9590, doi:10.1002/2015JD023818. <https://doi.org/10.1002/2015JD023818>.

Thompson, G., R. M. Rasmussen, and K. Manning, 2004: Explicit Forecasts of Winter

Precipitation Using an Improved Bulk Microphysics Scheme. Part I: Description and Sensitivity Analysis. *Mon. Weather Rev.*, **132**, 519–542, doi:10.1175/1520-0493(2004)132<0519:EFOWPU>2.0.CO;2. [http://dx.doi.org/10.1175/1520-0493\(2004\)132%3C0519:EFOWPU%3E2.0.CO](http://dx.doi.org/10.1175/1520-0493(2004)132%3C0519:EFOWPU%3E2.0.CO).

——, P. R. Field, R. M. Rasmussen, and W. D. Hall, 2008: Explicit Forecasts of Winter Precipitation Using an Improved Bulk Microphysics Scheme. Part II: Implementation of a New Snow Parameterization. *Mon. Weather Rev.*, **136**, 5095–5115, doi:10.1175/2008MWR2387.1. <http://dx.doi.org/10.1175/2008MWR2387.1>.

Tripoli, G. J., and W. R. Cotton, 1980: A Numerical Investigation of Several Factors Contributing to the Observed Variable Intensity of Deep Convection over South Florida. *J. Appl. Meteorol.*, **19**, 1037–1063, doi:10.1175/1520-0450(1980)019<1037:ANIOSF>2.0.CO;2. <http://journals.ametsoc.org/doi/abs/10.1175/1520-0450%281980%29019%3C1037%3AANIOSF%3E2.0.CO%3B2> .

Tzivion (Tzitzvashvili), S., G. Feingold, and Z. Levin, 1987: An Efficient Numerical Solution to the Stochastic Collection Equation. *J. Atmos. Sci.*, **44**, 3139–3149, doi:10.1175/1520-0469(1987)044<3139:AENSTT>2.0.CO;2. [https://doi.org/10.1175/1520-0469\(1987\)044%3C3139:AENSTT%3E2.0.CO](https://doi.org/10.1175/1520-0469(1987)044%3C3139:AENSTT%3E2.0.CO).

Uijlenhoet, R., M. Steiner, and J. A. Smith, 2003a: Variability of Raindrop Size Distributions in a Squall Line and Implications for Radar Rainfall Estimation. *J. Hydrometeorol.*, **4**, 43–61, doi:10.1175/1525-7541(2003)004<0043:VORSDI>2.0.CO;2. [http://dx.doi.org/10.1175/1525-7541\(2003\)004%253C0043:VORSDI%253E2.0.CO](http://dx.doi.org/10.1175/1525-7541(2003)004%253C0043:VORSDI%253E2.0.CO).

——, ——, and ——, 2003b: Variability of Raindrop Size Distributions in a Squall Line and Implications for Radar Rainfall Estimation. *J. Hydrometeorol.*, **4**, 43–61, doi:10.1175/1525-7541(2003)004<0043:VORSDI>2.0.CO;2. [http://dx.doi.org/10.1175/1525-7541\(2003\)004%3C0043:VORSDI%3E2.0.CO](http://dx.doi.org/10.1175/1525-7541(2003)004%3C0043:VORSDI%3E2.0.CO).

Varble, A., and Coauthors, 2014: Evaluation of cloud-resolving and limited area model intercomparison simulations using TWP-ICE observations: 1. Deep convective updraft properties. *J. Geophys. Res. Atmos.*, **119**, 13,891–13,918, doi:10.1002/2013JD021371. <http://doi.wiley.com/10.1002/2013JD021371> .

Wacker, U., and C. Lüpkes, 2009: On the selection of prognostic moments in parametrization schemes for drop sedimentation. *Tellus A*, **61**, 498–511, doi:10.1111/j.1600-0870.2009.00405.x. <http://dx.doi.org/10.1111/j.1600-0870.2009.00405.x>.

Walko, R. L., W. R. Cotton, M. P. Meyers, and J. Y. Harrington, 1995: New RAMS cloud microphysics parameterization part I: the single-moment scheme. *Atmos. Res.*, **38**, 29–62.

Wang, L.-P., and W. W. Grabowski, 2009: The role of air turbulence in warm rain initiation. *Atmos. Sci. Lett.*, **10**, 1–8, doi:10.1002/asl.210. <http://doi.wiley.com/10.1002/asl.210> .

——, O. Ayala, S. E. Kasprzak, W. W. Grabowski, L.-P. Wang, O. Ayala, S. E. Kasprzak, and W. W. Grabowski, 2005: Theoretical Formulation of Collision Rate and Collision Efficiency of Hydrodynamically Interacting Cloud Droplets in Turbulent Atmosphere. *J. Atmos. Sci.*, **62**, 2433–2450, doi:10.1175/JAS3492.1. <http://journals.ametsoc.org/doi/abs/10.1175/JAS3492.1> .

——, ——, B. Rosa, and W. W. Grabowski, 2008: Turbulent collision efficiency of heavy particles relevant to cloud droplets. *New J. Phys.*, **10**, 075013, doi:10.1088/1367-

2630/10/7/075013. <http://stacks.iop.org/1367->

2630/10/i=7/a=075013?key=crossref.5563f6394e6c9d714651ce5e3b75c3f7 .

Woods, J. D., and B. J. Mason, 1964: Experimental determination of collection efficiencies for small water droplets in air. *Q. J. R. Meteorol. Soc.*, **90**, 373–381,

doi:10.1002/qj.49709038602. <http://doi.wiley.com/10.1002/qj.49709038602> .

Yuter, S. E., and R. A. Houze, 1997: Measurements of Raindrop Size Distributions over the

Pacific Warm Pool and Implications for Z–R Relations. *J. Appl. Meteorol.*, **36**, 847–867,

doi:10.1175/1520-0450(1997)036<0847:MORSDO>2.0.CO;2.

[http://dx.doi.org/10.1175/1520-0450\(1997\)036%3C0847:MORSDO%3E2.0.CO](http://dx.doi.org/10.1175/1520-0450(1997)036%3C0847:MORSDO%3E2.0.CO).

Zhang, G., J. Vivekanandan, and E. Brandes, 2001: A method for estimating rain rate and drop

size distribution from polarimetric radar measurements. *IEEE Trans. Geosci. Remote Sens.*,

**39**, 830–841, doi:10.1109/36.917906. <http://ieeexplore.ieee.org/document/917906/> .

## Figure Captions:

**Figure 1:** Initial RSDs for each of the sensitivity simulations conducted. All of the RSDs are represented by gamma distributions with a constant mass mean diameter of 1.0 mm and number concentration of  $10 \text{ cm}^{-3}$ . The lines are labelled  $\nu\#$ , where  $\#$  is the value of the shape parameter shown by each line.

Figure 2: Collection efficiencies from Hall80, Long74, Pinsky01 at 1000, 750, and 500 hPa, and Wang09 at  $\epsilon = 100$  and  $400 \text{ cm}^2\text{s}^{-3}$  for one drop of radii a)  $10 \mu\text{m}$ , b)  $25 \mu\text{m}$ , c)  $50 \mu\text{m}$ , and d)  $100 \mu\text{m}$  and another drop as described on the abscissa.

Figure 3: The sounding (adapted from (Gaudet et al. 2006)) used for the horizontally homogenous initialization for the model in all simulations. The red line denotes temperature ( $^{\circ}\text{C}$ ) and the green line denotes dew point ( $^{\circ}\text{C}$ ).

Figure 4 : Surface accumulated precipitation ( $\text{kg m}^{-2}$ , shaded) after 130 minutes for all eight simulations where  $\nu = 2$  (top; a-d) and  $\nu = 10$  (bottom; e-h).

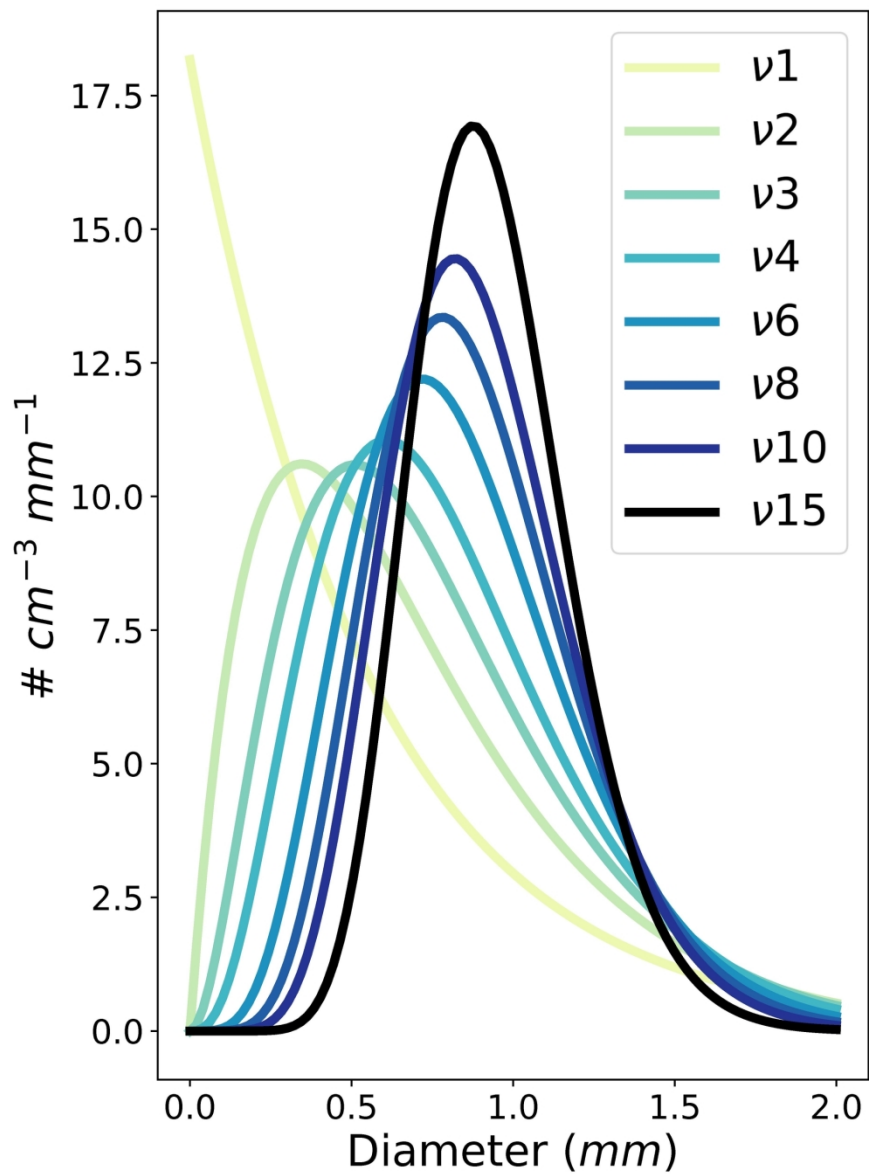
Figure 5: (a): Five minute average of grid-mean rain rate ( $\text{mm minute}^{-1} \text{ km}^{-2}$ ) as a function of time after the simulation start for all  $\nu = 2$  and  $10$  simulations (b): The same as in (a) but for total grid accumulated rainfall ( $\text{kg}$ )

Figure 6: Domain and time integrated rain amount ( $\text{mm}$ ) produced or removed by each microphysical process for all eight simulations where  $\nu = 2$  and  $\nu = 10$ . Cloud collection (red dots) relates to cloud and drizzle collision-coalescence with rain and autoconversion of cloud and drizzle to rain; collision melting (orange dots) is defined as the melting of all ice species into rain through the collision of such ice species with the liquid species; other melting (blue dots) is all melting of ice into rain not counting collision melting; ice accretion (green dots) is rain being accreted by ice; and condensation and evaporation (purple dots) are shown as the net of these two processes for rain only. Positive numbers indicate the creation or sources of rain, and negative numbers indicate the removal or sinks of rain. The total (cyan dots) is the sum of all processes. Note that for the Pinsky $\nu$ 2 case, Collision Melting and Cloud Collection are almost equal which makes the Collision Melting dot nearly non-visible.

Figure 7: a) Five minute average of grid-mean rain rate ( $\text{mm minute}^{-1} \text{ km}^{-2}$ ) as a function of time after the simulation start. Precipitation did not begin accumulating at the surface until 40 minutes after initialization. b) Total sum accumulated rainfall ( $\text{kg}$ ) as a function of time for all simulations. Mean vertical profiles of c) raindrop mass mean diameter, d) raindrop number concentration, and e) rain mixing ratio averaged over rainy columns (defined as all columns with integrated rain mixing ratio  $>0.1 \text{ g m}^{-2}$ ; note that panel (d) uses a log scale on the abscissa) from 40 to 130 minutes after initialization. In (b)–(d), the cloud base (defined as the average lowest point with cloud mixing ratio  $> 0.1 \text{ g kg}^{-1}$ ) is denoted by the black dashed line and the environmental  $0^\circ\text{C}$  line is denoted by the blue dashed line. f) Minimum perturbation  $\theta_p$  over time ( $\text{K}$ )

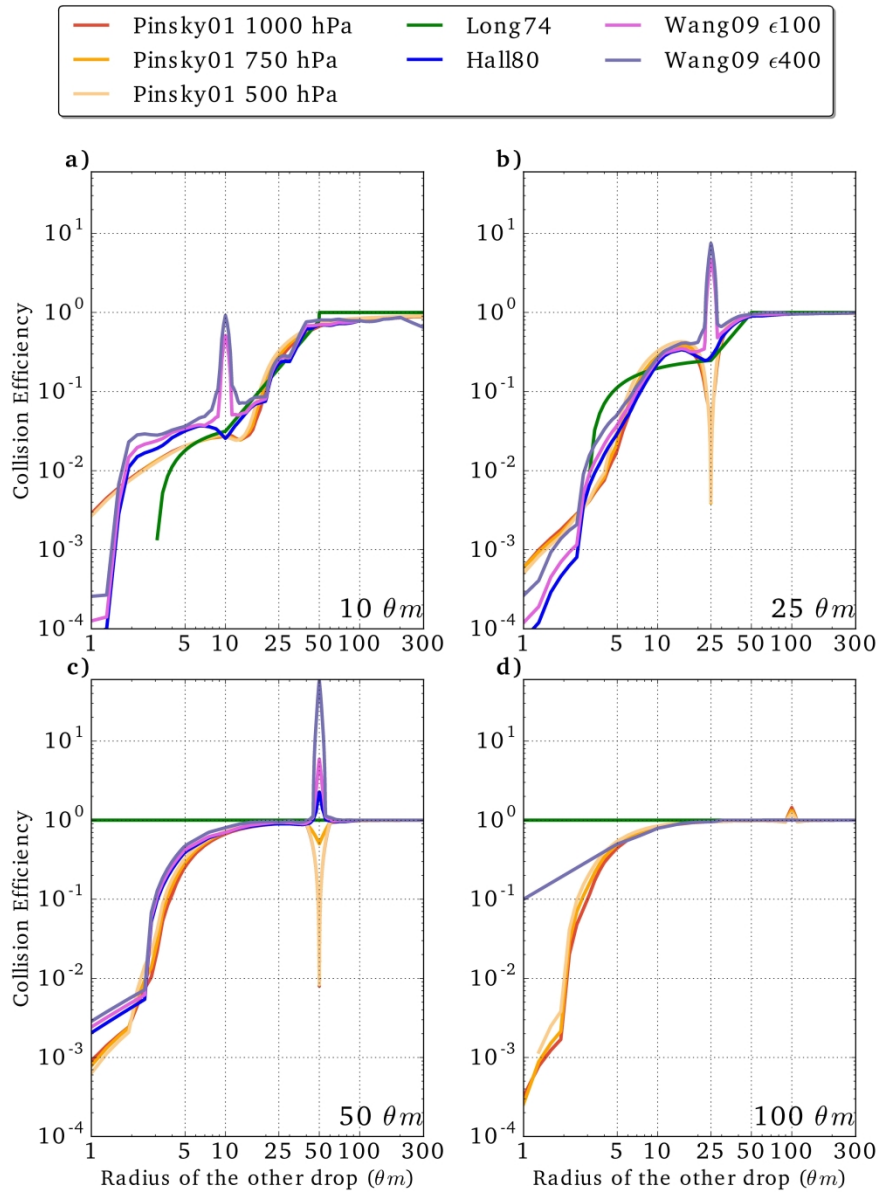
Figure 8: a) shows Domain and time integrated rain amount ( $\text{mm}$ ) produced or removed by each microphysical process, with colours the same as in Figure 6. b) shows  $v$  vs.  $v \left[ \frac{\Gamma(v)}{\Gamma(v+3)} \right]^{\frac{1}{3}}$  as used in the condensation/evaporation equation. c) shows the temporal and spatial mean vertical profiles of the number of raindrops self-collected per minute ( $\# \text{ kg}^{-1} \text{ min}^{-1}$ ) averaged over rainy points, where rainy points are defined as points containing a rain mixing ratio  $>0.1 \text{ g kg}^{-1}$ . Cloud base (as in Figure 7) is denoted by the black dashed line.

Figure 9: Panels a) and b) show accumulated hail precipitation at the ground ( $\text{kg m}^{-2}$ ) at 130 minutes for Longv2 (a; note that this panel should be dark as the maximum value is  $0.0003 \text{ kg m}^{-2}$ ) and Longv10 (b). The colour bar for panels a and b lies between them. Panel c shows the grid integrated total ice ( $\text{kg}$ ) over time. Panel d shows the horizontal mean hail vertical profile averaged over columns with an integrated total condensate value  $>1 \text{ kg m}^{-2}$  and has lines denoting cloud base and  $0^\circ\text{C}$  as in Figure 7(c,d,e).



**Figure 1:** Initial RSDs for each of the sensitivity simulations conducted. All of the RSDs are represented by gamma distributions with a constant mass mean diameter of 1.0 mm and number concentration of 10 cm<sup>-3</sup>. The lines are labelled ν#, where # is the value of the shape parameter shown by each line.

159x215mm (300 x 300 DPI)



**Figure 2:** Collection efficiencies from Hall80, Long74, Pinsky01 at 1000, 750, and 500 hPa, and Wang09 at  $\epsilon=100$  and  $400 \text{ cm}^2 \text{ s}^{-3}$  for one drop of radii a)  $10 \mu m$ , b)  $25 \mu m$ , c)  $50 \mu m$ , and d)  $100 \mu m$  and another drop as described on the abscissa.

293x398mm (300 x 300 DPI)

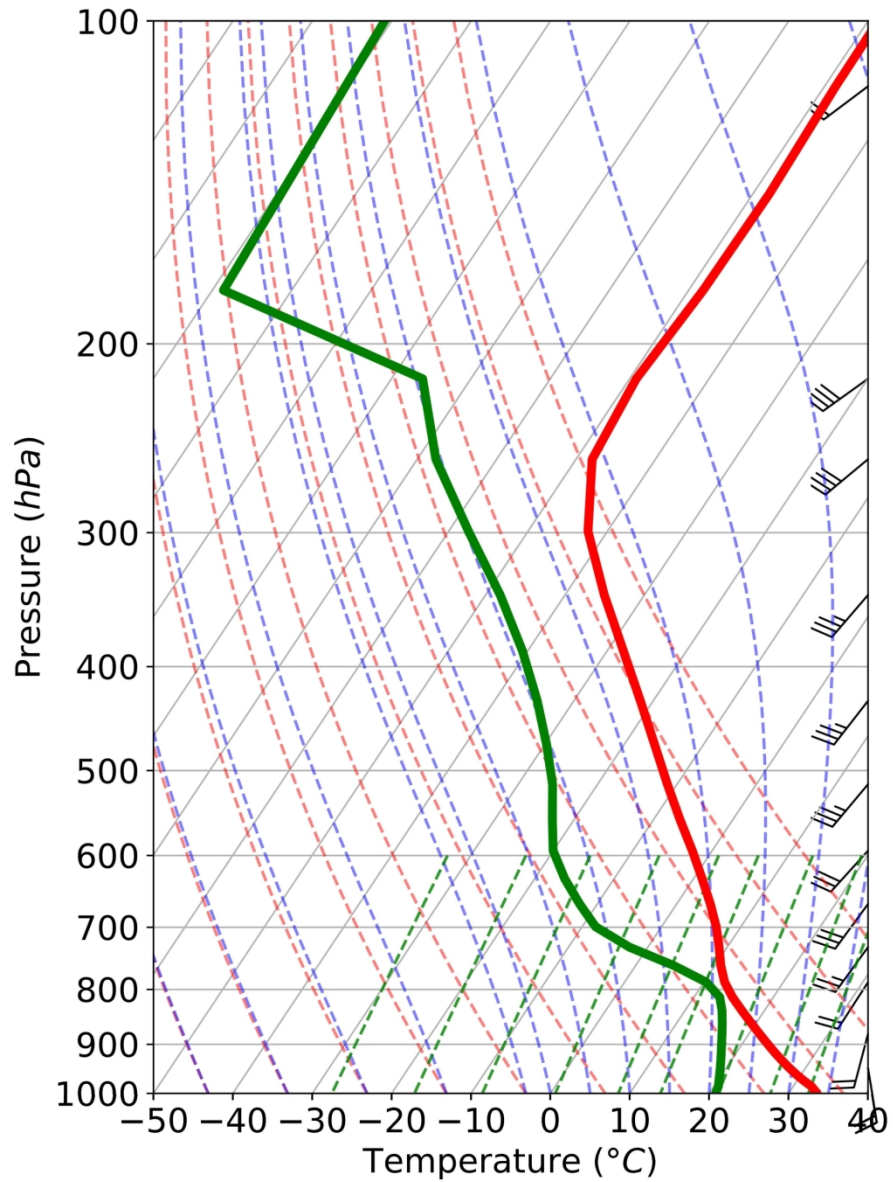


**Figure 3:** The sounding (adapted from (Gaudet et al. 2006)) used for the horizontally homogenous initialization for the model in all simulations. The red line denotes temperature (°C) and the green line denotes dew point (°C).

161x214mm (300 x 300 DPI)

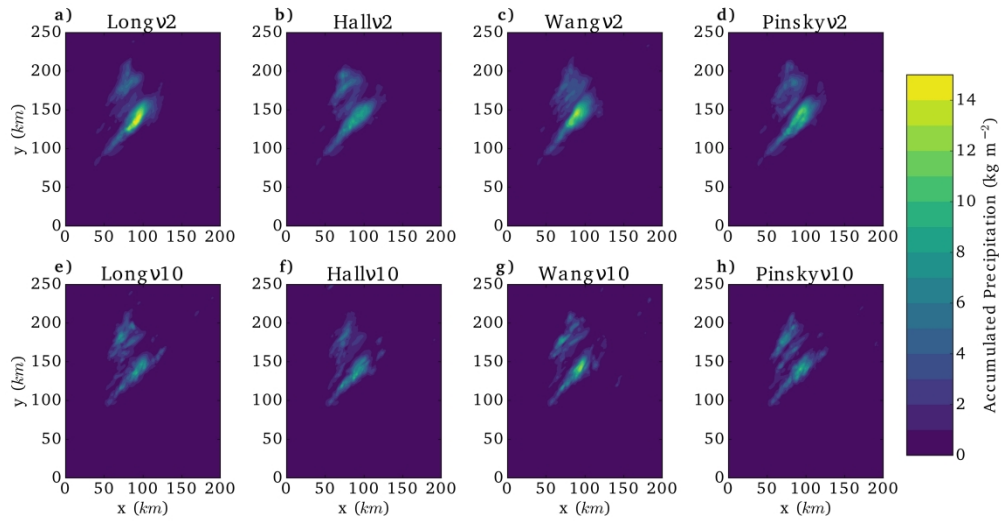


**Figure 4:** Surface Accumulated Precipitation ( $\text{kg m}^{-2}$ , shaded) after 130 minutes for all eight simulations where  $v=2$  (top; a-d) and  $v=10$  (bottom; e-h)

467x243mm (300 x 300 DPI)

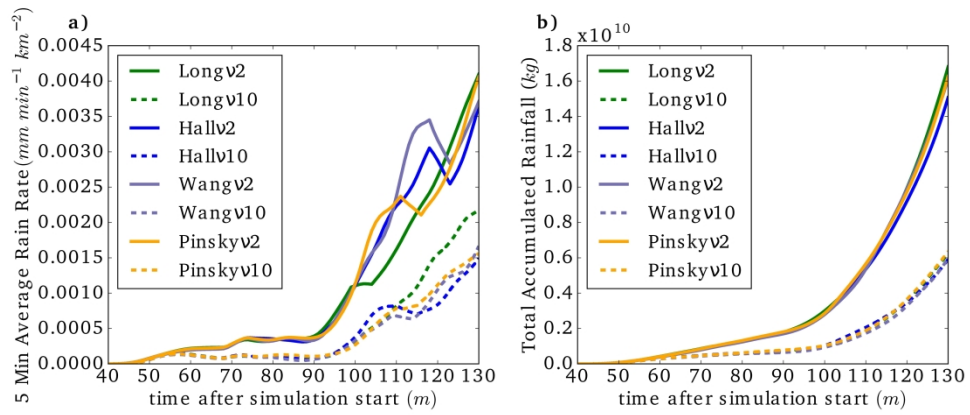


**Figure 5:** (a): Five minute average of grid-mean rain rate ( $\text{mm minute}^{-1} \text{ km}^{-2}$ ) as a function of time after the simulation start for all  $v=2$  and 10 simulations (b): The same as in (a) but for total grid accumulated rainfall (kg)

406x177mm (300 x 300 DPI)

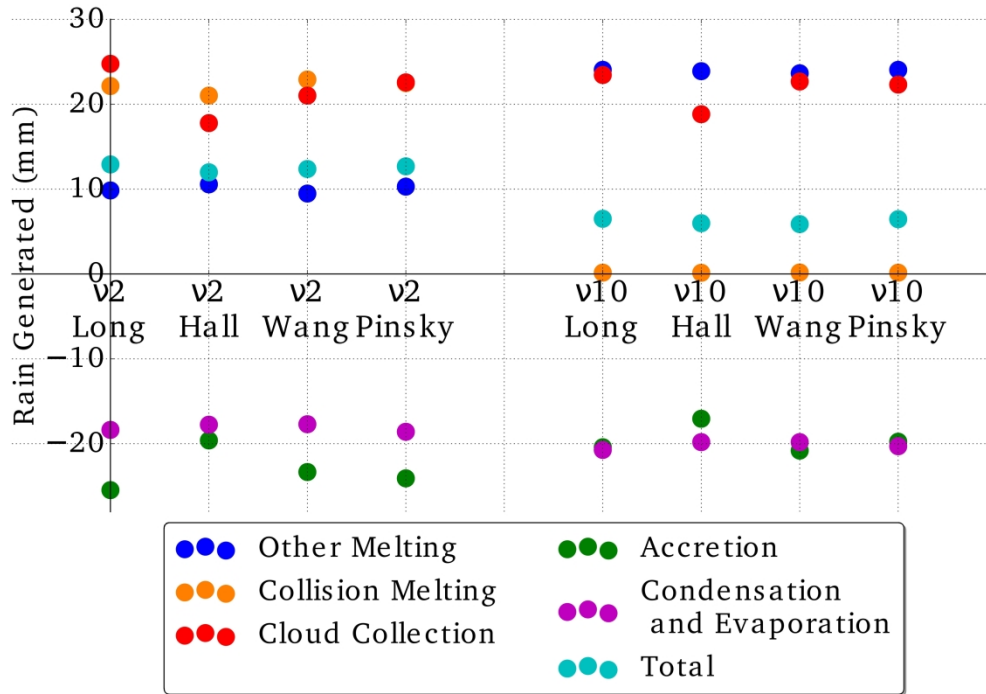


**Figure 6:** Domain and time integrated rain amount (mm) produced or removed by each microphysical process for all eight simulations where  $v=2$  and  $v=10$ . Cloud collection (red dots) relates to cloud and drizzle collision-coalescence with rain and autoconversion of cloud and drizzle to rain; collision melting (orange dots) is defined as the melting of all ice species into rain through the collision of such ice species with the liquid species; other melting (blue dots) is all melting of ice into rain not counting collision melting; ice accretion (green dots) is rain being accreted by ice; and condensation and evaporation (purple dots) are shown as the net of these two processes for rain only. Positive numbers indicate the creation or sources of rain, and negative numbers indicate the removal or sinks of rain. The total (cyan dots) is the sum of all processes. Note that for the Pinskyv2 case, Collision Melting and Cloud Collection are almost equal which makes the Collision Melting dot nearly non-visible.

359x252mm (300 x 300 DPI)

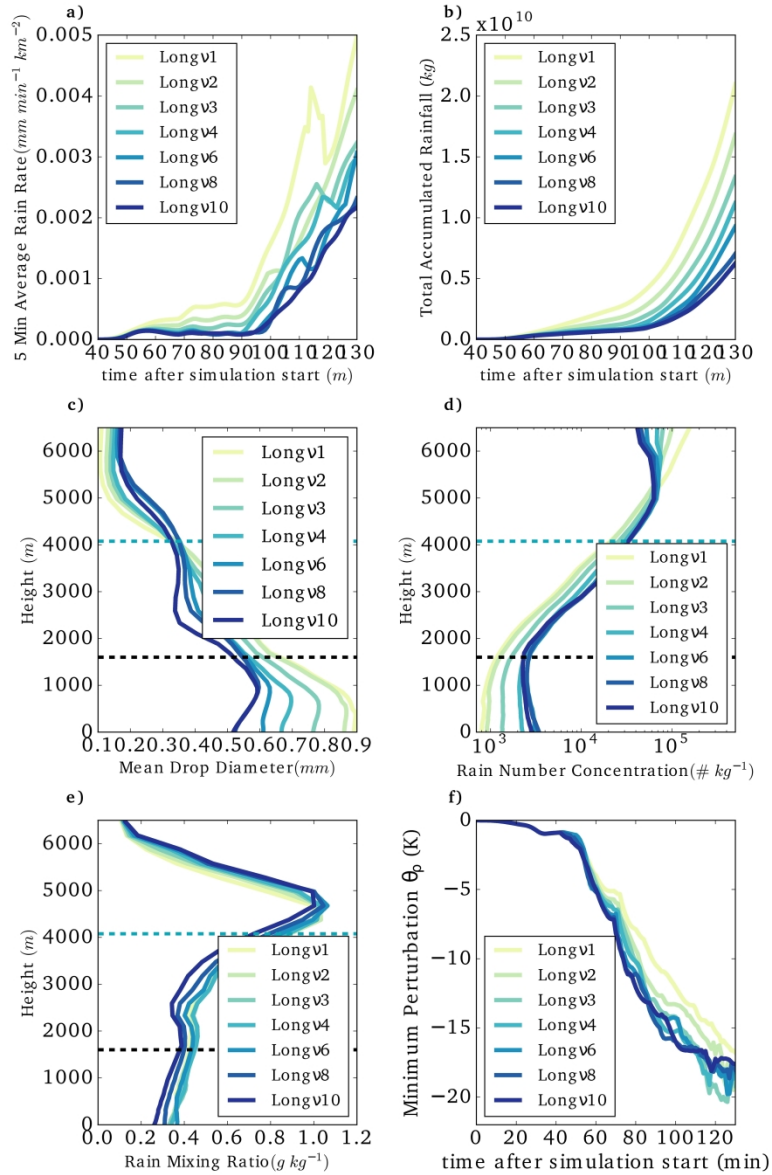


**Figure 7:** a) Five minute average of grid-mean rain rate ( $\text{mm minute}^{-1} \text{km}^{-2}$ ) as a function of time after the simulation start. Precipitation did not begin accumulating at the surface until 40 minutes after initialization. b) Total sum accumulated rainfall (kg) as a function of time for all simulations. Mean vertical profiles of c) raindrop mass mean diameter, d) raindrop number concentration, and e) rain mixing ratio averaged over rainy columns (defined as all columns with integrated rain mixing ratio  $> 0.1 \text{ g m}^{-2}$ ; note that panel (d) uses a log scale on the abscissa) from 40 to 130 minutes after initialization. In (b)–(d), the cloud base (defined as the average lowest point with cloud mixing ratio  $> 0.1 \text{ g kg}^{-1}$ ) is denoted by the black dashed line and the environmental  $0^\circ\text{C}$  line is denoted by the blue dashed line. f) Minimum perturbation  $\theta_p$  over time (K)

304x457mm (300 x 300 DPI)

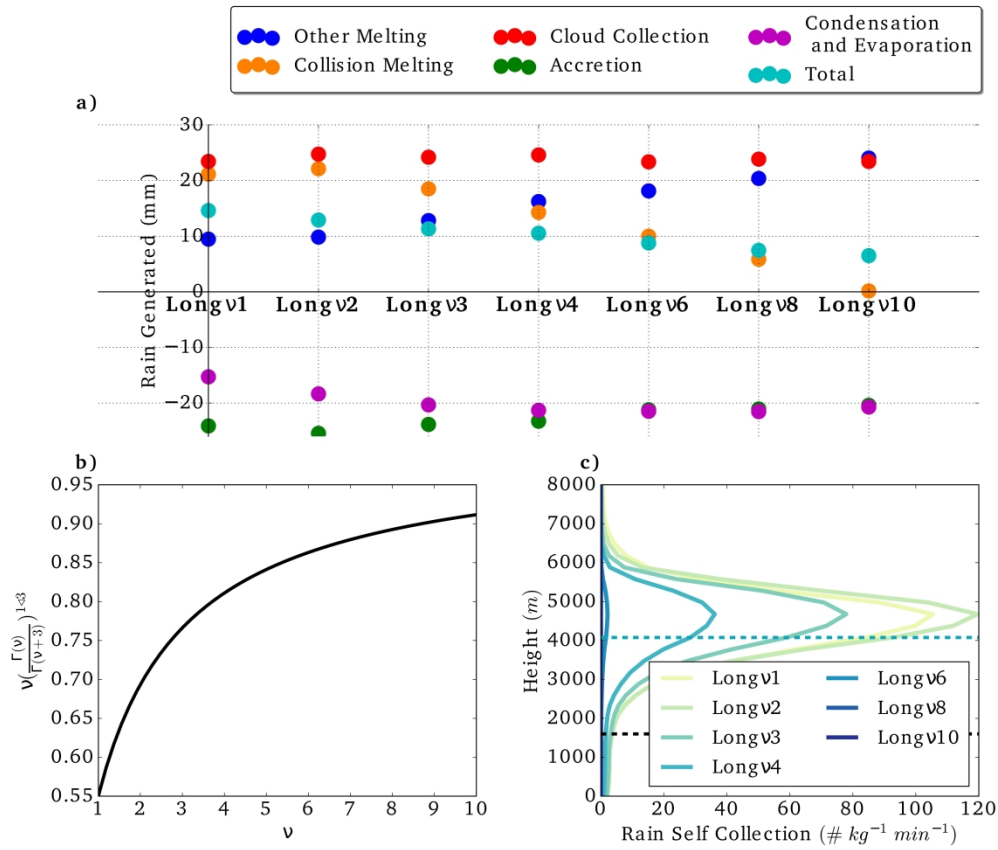


**Figure 8:** a) shows Domain and time integrated rain amount (mm) produced or removed by each microphysical process, with colours the same as in Figure 6. b) shows  $v$  vs.  $v[\Gamma(v)/\Gamma(v+3)]^{1/3}$  as used in the condensation/evaporation equation. c) shows the temporal and spatial mean vertical profiles of the number of raindrops self-collected per minute ( $\# \text{ kg}^{-1} \text{ min}^{-1}$ ) averaged over rainy points, where rainy points are defined as points containing a rain mixing ratio  $>0.1 \text{ g kg}^{-1}$ . Cloud base (as in Figure 7) is denoted by the black dashed line.

393x335mm (300 x 300 DPI)

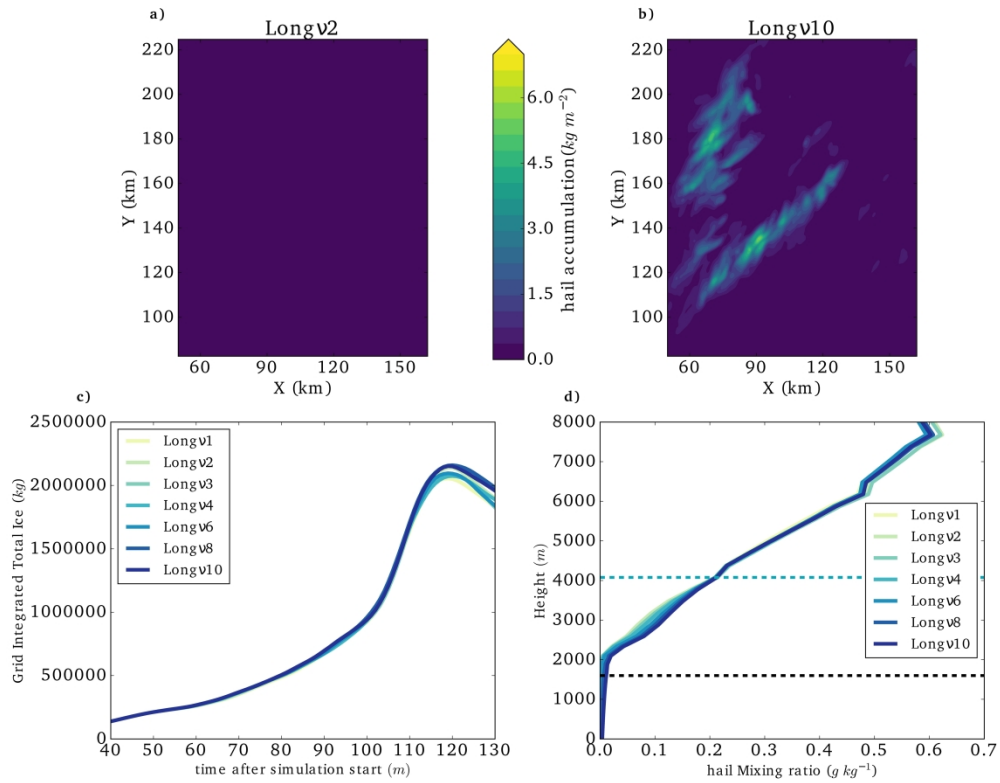


**Figure 9:** Panels a) and b) show accumulated hail precipitation at the ground ( $\text{kg m}^{-2}$ ) at 130 minutes for Longv2 (a; note that this panel should be dark as the maximum value is  $0.0003 \text{ kg m}^{-2}$ ) and Longv10 (b). The colour bar for panels a and b lies between them. Panel c shows the grid integrated total ice ( $\text{kg}$ ) over time. Panel d shows the horizontal mean hail vertical profile averaged over columns with an integrated total condensate value  $> 1 \text{ kg m}^{-2}$  and has lines denoting cloud base and  $0^\circ\text{C}$  as in Figure 7(c,d,e).

444x347mm (300 x 300 DPI)

**Table I:** Model setup information.

Model Configuration	Setting
Grid	$\Delta x=250\text{m}$ , 1000x800 grid points (250 km x 200 km); $\Delta z=25\text{m}$ at the surface; stretched to 300m over 92 vertical levels at a stretch ratio of 1.1
Initial Conditions	Horizontally Homogenous initial sounding modified from (Gaudet et al. 2006), shown in Figure 3
Initialization	Horizontal convergence zone (Loftus et al., 2008; Schumacher, 2009); initiated as an oval in the southwestern portion of the grid, with short and long axis lengths of 10 km and 20 km, respectively and vertical length of 1.2 km. The convergence was linearly increased to a magnitude of $5 \times 10^{-3} \text{ s}^{-1}$ at 10 minutes, after which the momentum forcing was terminated.
Radiation	None
Microphysics	RAMS 2 moment bin-emulating bulk scheme (Saleeby and van den Heever 2013; Saleeby and Cotton 2004; Walko et al. 1995); described in the text.
Time	Simulations run for 2.5 hours; analyzed for 130 minutes only. $\Delta t = 0.25\text{s}$

Boundaries	Lateral boundaries: open radiative. Top boundary: Rayleigh friction absorbing layer in the top 1.8 km. Bottom boundary: free slip.
Turbulence	Smagorinsky (1963)-type turbulence in the vertical and horizontal

**Table II:** The Experiments conducted in collection efficiencies (columns) and rain shape parameters (rows) along with the experiment name.

Rain Shape Parameter ( $\nu$ )	Long74 Collection Efficiencies	Hall80 Collection Efficiencies	Pinsky01 Collection Efficiencies	Wang09 Collection Efficiencies
1	Long $\nu$ 1	n/a	n/a	n/a
2	Long $\nu$ 2	Hall $\nu$ 2	Pinsky $\nu$ 2	Wang $\nu$ 2
3	Long $\nu$ 3	n/a	n/a	n/a
4	Long $\nu$ 4	n/a	n/a	n/a
6	Long $\nu$ 6	n/a	n/a	n/a
8	Long $\nu$ 8	n/a	n/a	n/a
10	Long $\nu$ 10	Hall $\nu$ 10	Pinsky $\nu$ 10	Wang $\nu$ 10